D^{*+} production in 7 TeV proton-proton and 5.02 TeV proton-lead collisions with ALICE

Erik Lumens (3588904)

Supervisors: A. Mischke, G. Luparello, S. LaPointe

June 17, 2013

Abstract

Sections 1-4 cover the theory needed to address this topic. The reader will find a brief introduction into Quantum Chromo-Dynamics and an interesting consequence of this theory: asymptotic freedom, which in turn leads to deconfinement. Next, the Quark Gluon Plasma is discussed. Finally, the D^* meson, the subject of this thesis, is studied by looking at its decay modes, how it is reconstructed and the track- and topological cuts needed for the yield extraction.
Section 5 focuses on the extraction of the D^* meson yield in proton-lead collisions at $\sqrt{s} =$ 5.02 TeV, the first step in the calculation of the nuclear modification factor in proton-lead interactions. Firstly, the best topological cuts per p_T bin are found. Particular attention is given to the lower p_T bin $[1, 2]$ GeV/c, where the signal extraction is more challenging due to a large combinatorial background due to random pairs. Next, we calculate the yield with a function which we fit to the data, using different fitting parameters. We also use a bin counting method. Finally, the systematic uncertainty is derived from this.
Section 6 looks at the feasibility of using $e - D^*$ correlations to study charm to beauty production in the beginning stages of the Quark Gluon Plasma. First, the correlation method is explained and afterwards a correlation is done for a MonteCarlo generated enhanced- and minimum bias sample for proton-proton collisions at 7 TeV. Finally, the process types gluon splitting, pair creation and flavour excitation are studied with this correlation method. The discussion then focusses on the feasibility of applying this method in order to determine the relative beauty fraction as well as the separation of $b\bar{b}$ and $c\bar{c}$ pairs.
Finally, in section 7 a conclusion is made. After this section the reader also finds the appendices.

Contents

1 Introduction

The Quark Gluon Plasma (QGP) is a hot, dense state of matter that is believed to have existed just moments after the Big Bang. It is fundamentally different from other states of matter, because the quarks (which are the building blocks of hadrons) are deconfined. Deconfinement means that the particle is allowed to exist as a free particle, instead of in a bound state. In other words, in the QGP quarks are found as single particles, rather than bound in a hadron. The result is a mixture of quarks and gluons (collectively called partons), with the latter being the force carriers for the strong force.
CERN, the European Organisation for Nuclear Research, is located in Geneva (Switzerland). Their flagship accelerator at the moment is the Large Hadron Collider (LHC). After protons or lead-ions go through a series of boosters, they are injected into the LHC, where they reach energies in the order of several TeV. They then collide with each other in one of the four main detectors: ATLAS, CMS, ALICE, LHCb. These detectors then study the underlying principles during or after the collisions to test existing theories and to find new physics.
ALICE (A Large Ion Collider Experiment) is optimized to study the matter created in high energy nucleus-nucleus collisions, namely the Quark Gluon Plasma. The temperature and density should be high enough for the creation of the QGP. Then, the plasma cools and the partons hadronize. We cannot directly measure the quarks, or other particles from the QGP, instead we measure the hadrons after hadronization.
In the early stages of the collision, there is enough energy available for the gluons to form heavy quarks like charm (c) and beauty (b). After the production c and b quarks travel through the medium. Contrary to light quarks, their production in the medium is sub dominant. Therefore, by studying heavy quark particles, particles that crossed the full medium are studied.
Heavy quarks cannot be directly measured but their production can be studied by reconstructing the hadronic decay channels of D mesons or by identifying electrons from the semi-leptonic decay of D and B mesons. The study of heavy-flavour lepton-D meson azimuthal correlations provides the means to estimate the beauty contribution to the heavy-flavour electron spectrum. In addition, they allow for the study of in-medium quark energy loss and modified fragmentation function in heavy-ion collisions.
In this work pp and p-Pb collisions are studied. The QGP is not expected to form in such collisions. The presence of the QGP in Pb-Pb collisions will result in different behaviour compared to proton-proton collisions because the medium will interact with the particles formed. The interactions that are a result of the QGP itself are called final-state effects. There are also cold nuclear effects (or initial-state effects), they are a result of the embedding of protons in a nucleus. With Pb-Pb collisions, both effects are measured at the same time. In order to disentangle these, a step between proton-proton and lead-lead collisions is studied: proton-lead collisions. Because there is no Quark Gluon Plasma formed after such a collision, only cold nuclear effects will have an influence on the created partons. Proton-proton collisions are, in turn, interesting to study collisions when no medium effects are present at all to study fundamental predictions of QCD. Thus, in order to study the QGP formed with Pb-Pb collisions the study of proton-proton and proton-lead collisions is necessary.
Because hard scattered partons interact with the QGP, they loose energy. It is therefore interesting to look at the yield of these partons and compare them to a base measurement in proton-lead collisions, to see how much the yield is suppressed and as such see what the presence of cold nuclear effects does to the yield. Because these partons cannot be observed directly, their decay daughters are studied. In this paper charged D^* mesons are studied. In section 5 the yield of these particles is studied in proton-lead collisions at $\sqrt{s} = 5.02$ TeV with real data.
In section 6 a feasibility study is done to see if the ratio of the heavy flavoured quarks charm

and beauty can be determined with proton-proton collisions. The method used is an azimuthal angle correlation between electrons and charged D^* mesons. Because of their decay mechanics, in theory these two particles can be separated based on a charge sign cut. The study is done on Monte Carlo samples at $\sqrt{s} = 7$ TeV.

2 Theory

In this section, the theory that is needed for our analysis is discussed. First, Quantum Chromo-Dynamics is briefly introduced. Next, the Quark Gluon Plasma is described together with the energy loss effects on partons travelling through this medium. Thirdly, the decay modes of the particle studied in this thesis, the charged D^*, are studied. Next, the reconstruction of charged D^*'s is discussed. Finally, track quality- and topological cuts for D^* candidates are treated.

2.1 Quantum Chromo-Dynamics

Quantum Chromo-Dynamics (QCD) is the theory that describes the interaction between colour-charged particles, i.e. quarks and gluons. There are six quarks: up (u), down (d), charm (c), strange (s), top (t) and beauty (b). These types are also called flavours. Only the lighter flavours (u and d) are stable, the rest of the flavours decay. This is why we only see particles composed of these two types in everyday life. Quarks have all kinds of properties, including spin, electric charge, mass, etcetera. An anti-quark has the same properties as its non-anti counterpart, only is of opposite charge sign. Quarks interact with each other through the strong force, the corresponding boson for this force is called the gluon. Quarks carry colour charge, roughly corresponding to electric charge in Electrodynamics. A difference with Electrodynamics is that photons, the boson corresponding to electrodynamics, does not carry an electrical charge, while the gluon does carry colour charge. Another difference is that there are three colour types in total, while there is only one type of electrical charge. These colour types are red, green and blue. The possible reactions in QCD are thus a bit richer than in Electrodynamics. The fundamental process of QCD is $q \rightarrow q + g$ (where we denote quark with q and gluon with g). We can show this process in what is called a Feynmann diagram, for this see figure 1. We demand

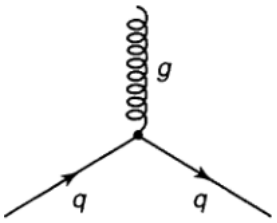

Figure 1: Feynmann diagram of $q \rightarrow q + g$ process. The time axis points to the right. [1]

of these processes that they are colour preserving, e.g. if a green d quark is turned into a red d quark, the gluon in the process depicted in figure 1 will be a gluon of type $\bar{g}r$. Notice that the flavour of the quark does not change in strong interactions. Gluons are bi-coloured, which means that they carry two different colour charges at the same time. Gluons can not only couple with quarks, but also with each other, forming what is called three-gluon and four-gluon vertices. In order to study the Quark Gluon Plasma we need to learn about two effects which appear in QCD: confinement and asymptotic freedom.

2.1.1 Asymptotic freedom

Asymptotic freedom is the property of quarks that they interact less when the energy increases or the distance decreases. The discovery of the effect is attributed to David Gross, Frank Wilczek and David Politzer who described it in a paper in 1973. They were awarded the Nobel Prize for physics in 2004 for this discovery. It is worth noting that Gerard 't Hooft (from the University of Utrecht) noted the effect in 1972 but did not publish. [2]
In order to explain the effect we would like to make an analogy with Quantum Electro Dynamics (QED). When two charged particles interact via QED, they are separated by a vacuum. Of course, a charged particle-antiparticle pair (e.g. an electron-positron pair) can be formed in this vacuum. Because there is an electric field, the vacuum becomes essentially polarized. The created pair will thus align itself as to diminish the electric field, thereby screening the electric field. The effect leads to a weaker electric field at any finite distance. When the distance decreases, we see less and less of the effects of the vacuum and thus less screening.
In QCD almost the same thing happens: virtual quark-antiquark pairs screen the strong field. This is not the only reaction that can happen, since gluons can interact with each other as well. They also have two colours instead of one. When gluon pairs are created they increase the colour field and change its colour. This is called anti-screening. It is now the question which of these two effects dominates the most in QCD, so that we can determine if screening or anti-screening dominates in Quantum Chromo Dynamics. Roughly, this depends on the number of different flavours of quarks. In any theory where $11n > 2f$, with n the number of colours and f the number of flavours, anti-screening effects will dominate over screening effects. In the case of Quantum Chromo-Dynamics there are three kinds of colours and six types of flavours, so indeed anti-screening will dominate. This makes the theory asymptotically free. The effective colour field decreases with the decrease of the distance between particles, because less gluons can appear in the intermediate medium.

2.1.2 Confinement

Deconfinement is a particular phenomenon which belongs to a phase. It states that particles can exist as free excitations, instead of only in bound states. An example for a phase with this property for quarks and gluons is the Quark Gluon Plasma, in which quarks are allowed to move more than one femtometer away from each other (where one femtometer is roughly the size of a hadron). Confinement on the other hand means that particles can only exist in bound states. Quarks are confined at low energies, meaning that they only exist in bound states. If we would like to seperate two static quarks, this would cost an infinite amount of energy. This is due to the force-carrying gluons exhibiting colour charge. The gluons field forms strings of colour charge. This means that the force that holds the quarks together is constant over any distance. Thus that it would be more beneficial for the system to create a quark-antiquark pair so as to get two neutral colour pairs. This process is illustrated in figure 2. This is the reason why we do not observe quarks directly in particle accelerators. If the energy is to low, they would already have bonded with each other.

2.2 Quark Gluon Plasma

According to lattice QCD calculations, at a temperature of about 170 MeV a phase transition takes place from a hadronic state to a state of quasi-free quarks and gluons, called Quark Gluon Plasma (QGP). The universe is believed to have been in this state starting about 10 picoseconds after the Big Bang and lasting for about 10 microseconds. The conditions needed for this state of matter are recreated by colliding heavy ions with each other. The goal is to obtain a system

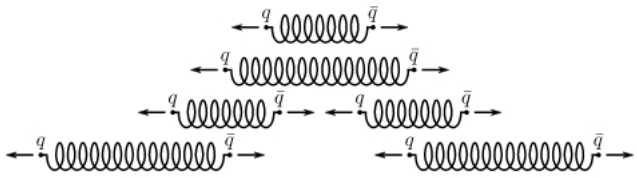

Figure 2: Illustration of what happens when separating two static quarks. The colour field produces a quark pair. [1]

with a large amount of particles, and local equilibrium. In this way the system can be described through thermodynamic quantities like the entropy, pressure, energy, temperature and their equation of state.
Because heavy quarks are so massive ($m > 1.2$ GeV/c^2), they are expected to be created in the early stages of the collision, in hard parton-parton scattering processes. They traverse the medium and interact with it.
In the QGP, partons loose energy due to elastic collisions with the medium constituents and due to gluon radiation.
If the Pb-Pb case were just a superposition of seperate pp events, no effects of the QGP would be observed. We describe this difference by the nuclear modification factor R_{AA}, which is defined as the ratio between the p_{T} spectrum of particles in Pb-Pb collisions and those of proton-proton collisions (where the number of protons is scaled to match the number of particles in the nucleus-nucleus collision). In mathematical form, it is defined as follows:

$$R_{AA} = \frac{1}{\langle N_{bin} \rangle} \frac{d^2 N_{Pb-Pb}/dp_{\mathrm{T}}dy}{d^2 N_{pp}/dp_{\mathrm{T}}dy},$$

where N_{bin} is the number of binary (nucleon-nucleon) collisions in the Pb-Pb collision and y is the rapidity, defined as:

$$y = \frac{1}{2} \log \left(\frac{E + p_z}{E - p_z} \right).$$

R_{AA} is called the nuclear modification factor and it describes the interaction of the particles with the medium. If $R_{AA} = 1$, we can see the collision as an independent superposition of pp collisions. If there is an interaction with the medium, the R_{AA} value will drop to $R_{AA} < 1$. Partons in the QGP are subjected to both cold nuclear effects and hot nuclear effects, these will alter the R_{AA}. Examples of cold nuclear effects include the Cronin effect and nuclear shadowing. When two nuclei collide there are multiple interactions within these nuclei and this causes broadening of the parton's transverse momentum. Nuclear shadowing has its origin in the difference in nuclear structure of a nucleus and a superposition of their nucleons. This causes the R_{AA} to drop.
The study of proton-lead collisions allows for a disentanglement of initial-state effects and final-state effects, because the latter only have an effect when a QGP is formed. In figure 3 the R_{AA} of D mesons measured by the ALICE collaboration is showed on the left. On the right, predictions for the R_{pA} at RHIC energies are shown. On the left, it is clear that at low tranverse momentum the data and models do not yet coincide. Low p_{T} is therefore important and will be dealt with accordingly during the analysis done in this thesis. Figure 4 gives a comparison

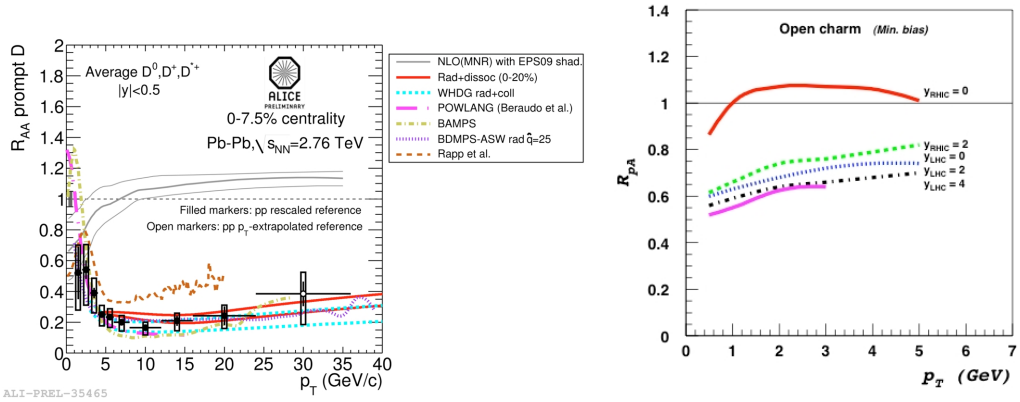

Figure 3: The left panel shows the nuclear modification factor R_{AA} for particles containing heavy charm quarks in the QGP. The data obtained using Pb-Pb collisions in the LHC are compared to energy loss models due to final-state effects (coloured curves). Grey curves represent model calculations with only initial-state shadowing. The right plot of the figure shows predictions from the so-called Colour Glass Condensate model, which describes cold nuclear effects on the R_{pA} of particles containing charm at different kinimetical ranges. [5–15]

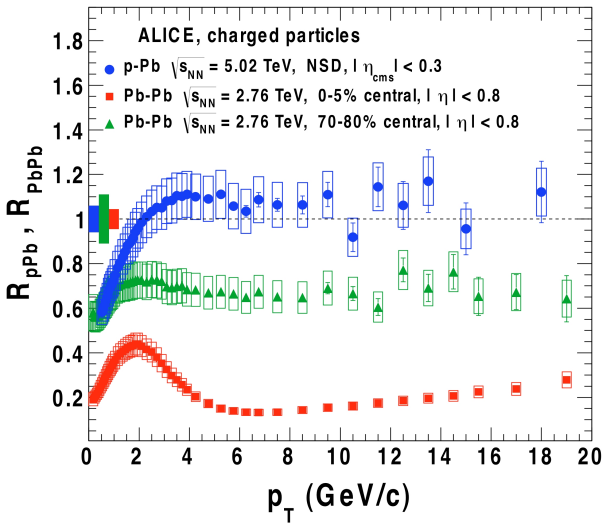

Figure 4: Nuclear modification factor at mid-rapidity for charged particles in proton-lead and lead-lead collisions, as measured by ALICE. [16]

of the measured R_{AA} and R_{pA} for charged hadrons. The R_{pA} is bigger than one at p_{T} values greater than 2 GeV/c, thus pointing towards the conclusion that the strong suppression observed in Pb-Pb collisions is a final-state effect.

2.3 Decay modes

D mesons are the lightest particles containing charm quarks. There are four isospin-states for the D mesons: D^0 ($c\bar{u}\uparrow\downarrow$), D^{*+} ($c\bar{d}\uparrow\uparrow$), D^{*0} ($c\bar{u}\uparrow\uparrow$) and D^+ ($c\bar{d}\uparrow\downarrow$). These are joined by their respective anti-particles. The D^{*+} (and D^{*-}) have a very narrow peak (96 ± 22 keV/c^2) when studied with the invariant mass method and this makes them easier to detect than most other D mesons. Especially in Pb-Pb collisions, where the background will be large. The D^* particles have a rest mass of 2010.28 ± 0.13 MeV/c^2. The D^{*+} has the following decay channels: [4]

- $D^{*+} \rightarrow D^0\pi_s^+$ $\qquad (\Gamma_i/\Gamma = 67.7 \pm 0.5\%)$
- $D^{*+} \rightarrow D^+\pi_s^0$ $\qquad (\Gamma_i/\Gamma = 30.7 \pm 0.5\%)$
- $D^{*+} \rightarrow D^+\gamma$ $\qquad (\Gamma_i/\Gamma = 1.6 \pm 0.4\%)$

π_s denotes a soft pion, which is a pion with small momentum in the order of 39 MeV/c^2 in the D^{*+} rest frame. The D^{*-} has the same decay channels, but with opposite signs. The first decay channel is the most interesting, not only because of the higher chance of occurring, but also because the soft pion is electrically charged and can be detected by the ITS. The D^{*+} has a short lifetime: $(6.9 \pm 1.9) \times 10^{-21}$ s. This has a consequence that its daughters (D^0 and π_s^+) look like they are coming from the interaction point, due to the particle's extremely short path from the primary vertex. The D^0 meson is also not stable and has a mean lifetime of $\tau = (4.101 \pm 0.015) \times 10^{-13}$ s. Thus the secondary vertex is expected at a distance $c\tau = 123\mu$m from the interaction point. The rest mass of the particle is 1864.63 ± 0.14 MeV/c^2. The most common decay channel (which is the one studied in this thesis) is: [4]

$$D^0 \rightarrow K^-\pi^+ \qquad (\Gamma_i/\Gamma = 3.89 \pm 0.05\%).$$

Thus the total branching ratio of the studied decay channel $D^{*+} \rightarrow D^0\pi_s^+ \rightarrow (K^-\pi^+)\pi_s^+$ is $\Gamma_i/\Gamma = 2.63\%$.

2.4 Reconstruction

The reconstruction algorithm first searches for D^0 candidates. It does this by first looping over all tracks belonging to negative- and positive tracks and thus matching π and K candidates. This results in a combinatorial background, since these candidates are not all pions and kaons. The algorithm tries to diminish the background by applying numerous quality cuts, for example η in a certain range, tracks should be good candidates for π and K and so on. Two candidates that are matched in this way are henceforth denoted as x_1 and x_2, with x_1 the kaon candidate and x_2 the pion candidate. So one of them is positive, the other one negative. Next, the invariant mass of this pair is calculated and compared to the D^0 invariant mass window for a specific p_T range. If the invariant mass lies within this window, the track is accepted for further analysis. If not, it is discarded. The invariant mass for the pair x_1 and x_2 is calculated as follows:

$$M_{x_1,x_2} = \sqrt{(E_K + E_\pi)^2 - (\boldsymbol{P}_{\boldsymbol{x_1}} + \boldsymbol{P}_{\boldsymbol{x_2}})^2},$$

with $E_K = \sqrt{m_K^2 + \langle \boldsymbol{P}_{\boldsymbol{x_1}}, \boldsymbol{P}_{\boldsymbol{x_1}} \rangle}$ and $E_\pi = \sqrt{m_\pi^2 + \langle \boldsymbol{P}_{\boldsymbol{x_2}}, \boldsymbol{P}_{\boldsymbol{x_2}} \rangle}$. What is left now is finding the soft pion. The algorithm now loops over all remaining tracks which have a plus- or a minus sign, depending on if the candidate for the K was positive or negative, respectively. The particle associated with this soft pion is denoted by x_3. After some quality cuts, that minimize the combinatorial background, the invariant mass of the particles x_1, x_2 and x_3 together is calculated:

$$M'_{x_1,x_2,x_3} = \sqrt{(E_K + E_\pi + E_{\pi_s})^2 - (\boldsymbol{P}_{\boldsymbol{x_1}} + \boldsymbol{P}_{\boldsymbol{x_2}} + \boldsymbol{P}_{\boldsymbol{x_3}})^2}.$$

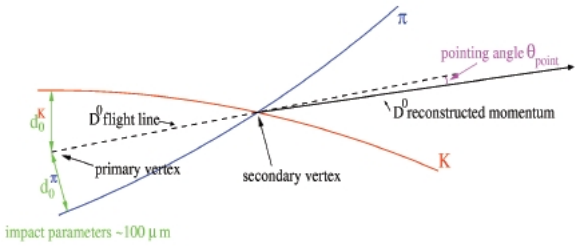

Figure 5: Schematic overview of the topology of a $D^0 \to K\pi$ decay, with a number of cut parameters. [3]

This number is compared with the invariant mass of the D^* and only if this number lies in a certain range these tracks are accepted. The D^* and D^0 have almost the same mass. It is thus better to look at the invariant mass difference between the two. This is because the uncertainties in the determination of the momenta of the kaon and the pion cancel, leading to a better resolution. Thus, we look at the invariant mass difference $\Delta M = M'_{x_1,x_2,x_3} - M_{x_1,x_2}$. Since the invariant masses of the D^0 and D^* are known, we expect the peak for ΔM, where the signal is, around 145.5 MeV/c^2.

2.5 Track quality cuts

The K and π candidate tracks are required to have:

- TPC refit and at least 70 clusters in TPC
- ITS refit
- A minimum of one hit in SPD

The soft pion also has a requirement, namely:

- A minimum of one hit in SPD

2.6 Topological cuts for the D^* reconstruction

Topological cuts are applied in order to reduce the combinatorial background. A D^0 decay vertex is depicted in figure 5. The particle travels from the interaction point, which is called the primary vertex, to the point where it decays, which is called the secondary vertex. The reason the topological cuts are applied on the D^0 flight path and not on the D^* path is because the D^* has a short decay length due to the fact that it decays via a strong process. The longer decay length of the D^0 allows for the reconstruction of the D^0 flight path. A list is presented, with the most important topological cut parameters.

- The kaon and pion tracks are extrapolated based on momentum of the detected particles. The impact parameter for kaon and pion is denoted as d_0^K and d_0^π, respectively, and is defined as the distance of closest approach between the primary vertex and the extrapolated track of the respective particle. These parameters themselves are important topological cut parameters, but their product $d_0^K \times d_0^\pi$ is important as well. This is because the distribution of the product will be symmetric around zero for background, but not for signal. This is because the background is completely random, while for candidates the two d_0's should have opposite sign.

- Next, the pointing angle θ_{point} is discussed. There are two ways to calculate flight line of the D^0. First, the primary- and secondary vertex can be connected and this line should point in the direction of the flight line of the D^0. Second, from the momentum of π and K the momentum of the D^0 can be calculated. These two directions should be the same, but because of resolution of the detector they are not. The angle between these two flight lines is the pointing angle θ_{point}. The next parameter used as a cut is the cosine of the pointing angle: $\cos(\theta_{\text{point}})$. This parameter is more constant for background and is peaked at one for the signal. The $\cos\theta_{\text{point;XY}}$ is closely related to this parameter; it is the cosine of the pointing angle in the XY plane. Here only the transverse components are evaluated.
- The next parameter discussed is the distance of closest approach (dca), defined as the minimum distance between the reconstructed track of the pion and the kaon. In general, if the two tracks are not connected to D^* candidates the dca will be large.
- Another topological cut can be done on the p_{T} of the π, K and π_s, respectively.
- Another angle proves to be useful: the decay angle θ^*, defined as the angle between the momentum of the π in the rest frame of the D^0 and the flight line of the D^0 in the lab frame. The $\cos\theta^*$ is evenly distributed for the background, while the $\cos\theta^*$ tends to ± 1.
- Next is the normalized decay length (NDL). This is the decay length of the candidate, divided by the error on this decay length.
- Lastly, a particle identification cut, or PID cut, can be used. In this thesis, a PID cut of 3σ is used whenever mentioned and this means that a particle is identified within a certainty of 3σ. This cut is expected to have a strong influence on background, but not so much on signal.

The values of the cuts depend on the p_{T} value of the candidates. The cuts are much tighter at low p_{T}, where the combinatorial background is larger, than at high p_{T}, where the combinatorial background is lower.

3 Research Questions

3.1 D^{*+} yield extraction

In section 5 the following question is answered:

- What is the production yield of charged D^* mesons in p-Pb collisions?

This question is answered by first finding topological cuts that maximize the yield of the charged D^* meson in each p_T bin. The method used is varying the different topological cut parameters and searching for the best set of cuts (one that maximizes the significance). This is especially difficult in the p_T range $1 - 2$ GeV/c, because of the large combinatorial background from random pairs. Therefore, a deep study of this particular bin is necessary. Next, the systematic error on this yield extraction method is studied. First, a PID check is applied to see how well it decreases the background and increases the signal over background ratio. The stability of the yield extraction method is analysed by varying different fitting parameters for the background function and the background function itself. A bin counting method is also used to look how the yield changes. This study is done by looking at two real data samples, containing proton-lead collisions at $\sqrt{s} = 5.02$ TeV for a total of about 120 million events.
As said before, this research subject is a fundamental step towards the R_{pA}, because when compared to proton-proton collisions the modification of the yield due to cold nuclear effects can be measured. In this way, initial- and final-state effects can be effectively disentangled.

3.2 $e - D^{*+}$ azimuthal angular correlations

The aim of section 6 is to answer the following question about the electron-D^* correlation:

- Is the $e-D^*$ correlation method a valuable method to distinguish between- and seperate $c\bar{c}$ and $b\bar{b}$ events in pp and Pb-Pb collisions?
- Do the selections for the process types such as gluon splitting, flavour excitation and pair creation work as expected and can this be determined using $e-D^*$ correlations?

To achieve this goal, first Monte Carlo generated proton-proton datasets are studied. After checking the feasibility of the usefulness of this correlation by using a heavy flavour enhanced Monte Carlo sample, a Minimum Bias Monte Carlo sample is used to determine whether this correlation can help in distinguishing between $b\bar{b}$ and $c\bar{c}$ events with real data. If this is successful as well, the last step will be to look at proton-proton data samples. The correlation studies will be performed with the ALICE experiment at the Large Hadron Collider (LHC). The main sub-detectors utilized for the analysis include the Inner Tracking System (ITS), the Time Projection Chamber (TPC), the Time Of Flight (TOF), and the Electromagnetic Calorimeter (EMCal). The heavy flavour enhanced sample provides more statistics compared to a minimum-bias Monte Carlo sample. The Monte Carlo samples are generated using PYTHIA, which generates the physics, and then Geant does the detector simulation for the ALICE detector. The reconstructed data is then used to identify particles. For the study of the process types, the previously mentioned enhanced data sample will be used. The electrons are selected so that they originate from one of these processes and then $\Delta\phi(e_{\mathrm{HF}},\mathrm{D}^*)$ correlations are used to check whether these selections work properly.

4 Experimental Setup

4.1 ALICE Detector

The ALICE detector is one of the four main detectos at the LHC, the others being ATLAS, CMS and LHCb. The dimensions of the detector are: 26 m in length, 16 m in width and 16 m in height. ALICE boasts a strong magnet which can deliver a field between 0.2 and 0.5 Tesla. The detector consists of two parts: a forward muon arm and a central barrel. The detector is build around a collision point of the LHC and build out of multiple layers, each layer detecting something different. There are a total of 17 subdetectors, of which we will describe the ones used for this study. The ALICE detector is depicted in figure 6.

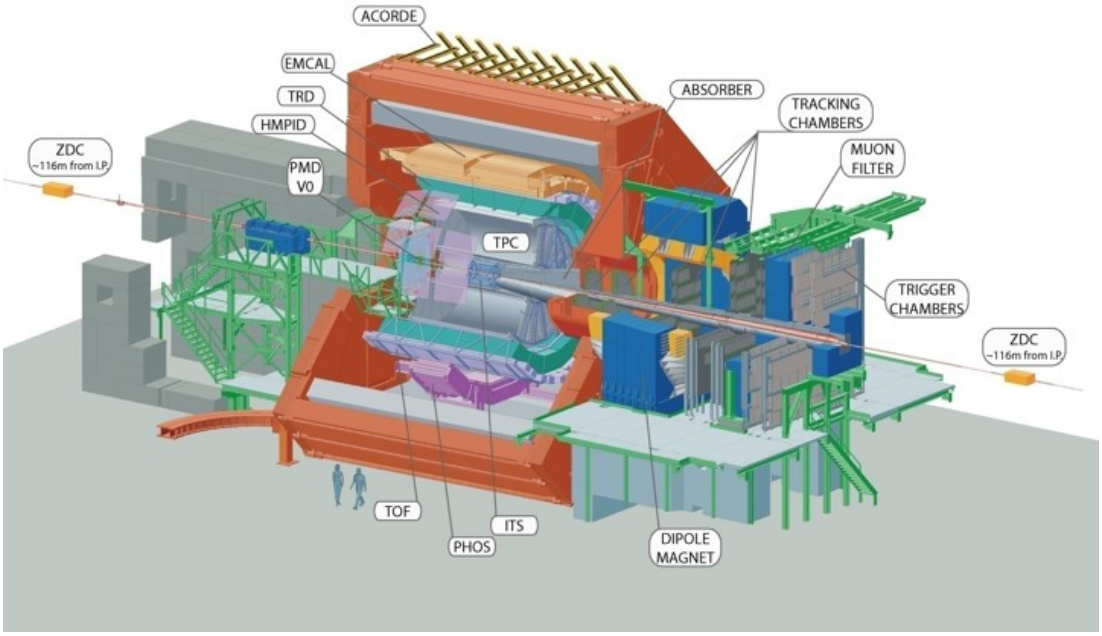

Figure 6: Layout of the ALICE detector.

4.1.1 Inner Tracking System

The Inner Tracking System or ITS consists of six cylindrical concentric layers. The whole detector covers for $|\eta| < 0.9$, with η or pseudo-rapidity a spatial coordinate defined as follows:

$$\eta = -\ln\left[\tan\left(\frac{\theta}{2}\right)\right],$$

with θ the angle between the particles path and the beam axis. The innermost layers cover up to $|\eta| < 1.98$. The inner two layers form the Silicon Pixel Detector (SPD). The two layers in the middle form the Silicon Drift Detector (SDD) and the outermost two layers form the Silicon Strip Detector (SSD). The main goals of the SPD are the determination of the primary vertex

and in the help with the measurement of the impact parameter of secondary tracks originating from the weak decays of strange, charm and beauty particles. Except for the SPD, all layers can identify particles via dE/dx measurements for non-relativistic particles. Thus the ITS is a stand-alone particle spectrometer, though at low p_{T}. Also particles with low momenta that have tracks that are to curved due to the magnetic field for the Time Projection Chamber to reconstruct can be identified with the ITS. The Time Projection Chamber will be discussed in the next section. Of course, when the ITS and the Time Projection Chamber work together, the resolution for particles with high p_{T} will also increase. The layout of the Inner Tracking System is depicted in figure 7.

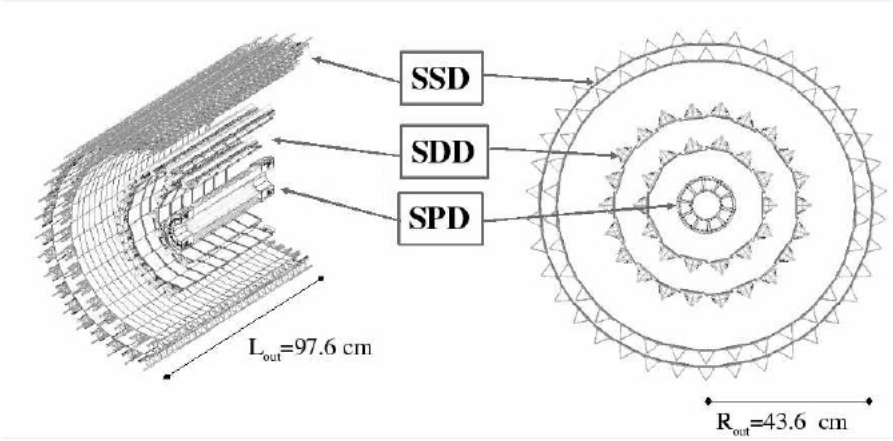

Figure 7: The layout of the Inner Tracking System.

4.1.2 Time Projection Chamber

The main functions of the Time Projection Chamber (TPC) are to provide track finding, measurements of the momentum of charged particle and particle identification. All of this in a p_{T} region bigger than 100 MeV/c and a pseudo-rapidity $|\eta| < 0.9$. The detector has a cylindrical shape, with a volume of 88 m^3. The detector is divided into two regions, both filled with a gas mixture of Ne, CO_2 and N_2. The active gas region ranges from 85 to 250 cm in the radial direction and 500 cm in the direction of the beam axis. An electrode is situated in the axial centre of the detector. The gas is put in an electric field, with voltages of 100 kV at electrode in the centre. A field cage was constructed to ensure that the electric field applied is uniform in the gas, that this electric field is isolated from the rest of the detector, and to have a mechanical structure which is stable and which can support the rest of the structure of the TPC. The layout of the TPC is depicted in figure 8.
When high energy particles travel through the TPC they ionize the gas by transmitting kinetic energy to the gas particles. These emit electrons. Because of the electric field, the electrons undergo an electric force which pushes them towards the end plates of the detectors, where the electron is detected and the resulting signal is amplified. Because a high energy particle ionizes a whole trace of gas particles and the emitted electrons all drift at the same speed towards the end plate, a 3D-image of the path trajectory can be reconstructed. The trace will be bend differently in the electric field, depending on the momentum and charge of the high energy particle. The higher the charge and the lower the momentum, the stronger the ionized path will be bended. The density of the ionization trail will also depend on the momentum and the kind of parti-

cle that caused the trail. There are effects which counter the precision of the Time Projection Chamber. Small mechanical or electrical errors in the field cage or in the readout chambers, the area where the detectors are situated, can give rise to a non-uniform electron drift. Temperature fluctuations and $E \times B$ effects (caused by the relative misalignment of the electric- and magnetic fields) can cause anomalies in the electron drift, which will cause them to stray from their ideal paths. To counter these two effects, a laser system has been build which can calibrate the drift field parameters. The lasers generate tracks inside the gas, which can then be used to make measurements of drift velocities.
The most important requirements that the TPC has to fulfil are, among others:

1. Track finding and matching with tracks from the ITS and TOF (efficiency $> 90\%$).
2. Measurement of the charged particles momentum (resolution between $1 - 2\%$ for low p_{T}, results depend on the applied magnetic field).
3. Particle identification ($\mathrm{d}E/\mathrm{d}x$ resolution $< 10\%$).
4. Two-track separation (resolution in relative momentum < 5 MeV$/c$) in the region $1 < p_t < 10$ GeV$/c$ and pseudo-rapidity $|\eta| < 0.9$.

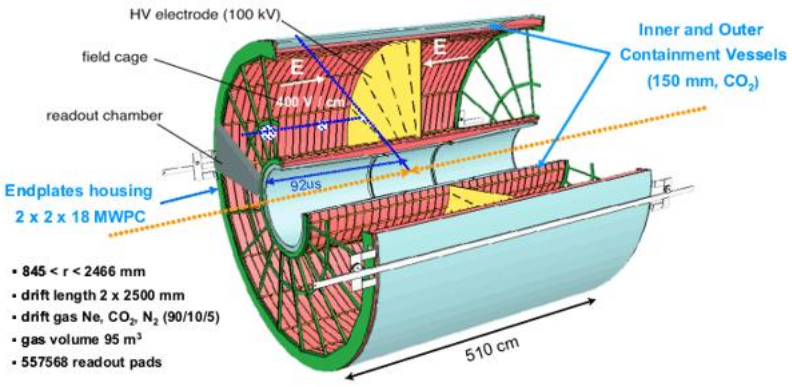

Figure 8: The layout of the Time Projection Chamber.

4.1.3 Electromagnetic Calorimeter

The Electromagnetic Calorimeter (EMCal) is a subdetector of ALICE which is designed to measure the energy of particles which interact primarily through the electromagnetic interaction. The detector greatly enhances ALICE's capabilities of measuring jets and high momentum photons and electrons. Since the ALICE detector has excellent tracking capabilities in a broad p_{T} range, the EMCal makes sure that jets, produced by heavy ion collisions in the LHC, can be studied. In the past only high-p_{T} hadrons in a jet could be identified. These interact the least with the rest of the medium so this is a pretty biased view on the situation. The EMCal can do full jet reconstructions. The acceptance of the EMCal for photons and neutral mesons is six times higher than the PHOS detector (also an electromagnetic calorimeter at the ALICE experiment, see figure 6). The measurements of heavy flavour production at high p_{T} provides a u, which is nique insight into jet quenching. The ALICE detector has good options for electron

measurements (TPC and TRD), the EMCal has the advantage for high p_{T} electrons ($p_{\mathrm{T}} > 10$ GeV/c) by a fast trigger system and hadron rejection. Figure 9 shows a part of the detector. The EMCal constitutes a cylindrical integration volume of about 110 cm in the radial direction, starting from about 450 cm from the beam line. In the direction of the beam the EMCal has a length of about 700 cm, which means that it covers the area for which $|\eta| < 0.7$. A particle enters the EMCal and hits the material constituting the detector, initiating a particle shower until the energy of the particles in the shower is to low. The change in temperature of the material is then measured, resulting in a measurement of the momentum of the particle. The direction of the particle can be determined, as well as the type of particle initiating the particle shower. The latter can be done by studying the shape of the shower.

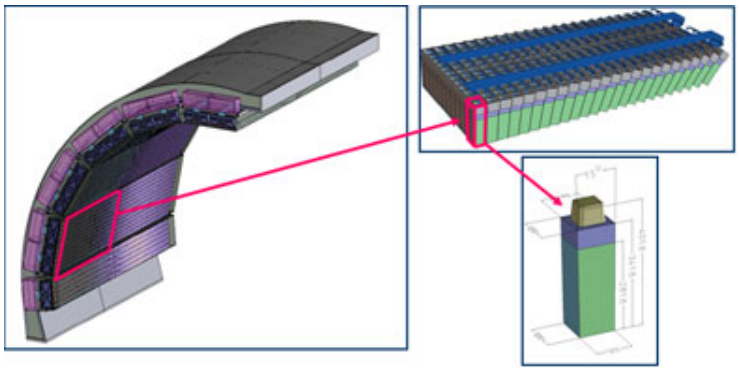

Figure 9: The layout of the Electromagnetic Calorimeter.

4.2 Data handling and computing

The Worldwide LHC Computing Grid (WLCG), is a network of computer centres, distributed over 36 countries and is the largest computer network as of 2012. The aim of this computing network is to provide resources to help analyse and distribute the enormous amount of data produced by the LHC each year. By 2012 over 300 trillion proton-proton collisions had been studied, at a rate of about 25 petabytes of data each year. The analyse done for this thesis are all done on this computing grid. After the analysis, together with the information about the dataset analysed, is submitted, the network calculates everything on one or multiple sites.

5 D* yield extraction in 5.02 TeV proton-lead collisions

5.1 Systematic Error Sources

5.1.1 Invariant mass fitting method

The D* candidates that passed the various topological cuts are plotted with respect to their invariant mass value. This plot is then fitted to obtain the D* raw yield. The function used to describe the peak of the invariant mass distribution is:

$$f_{\text{Gauss}}(x) = \frac{p_2 e^{\frac{-(x-p_0)^2}{2p_1^2}}}{\sqrt{2\pi}p_1},$$

with p_0, p_1 and p_2 the fitting parameters. Since there are three parameters for the peak, rebinning has to be adjusted according to how many points there are under the peak. If there are three points or less the Gaussian can not be determined properly. This peak function is added to the background function, which will be varied in this thesis. The standard function describing the background is:

$$f_{\text{thresh}}(x) = p_3(x - m_\pi)^{p_4},$$

which is a threshold function with m_π the mass of the pion (0.1395 GeV/c^2) and p_3 and p_4 fitting parameters. Our standard fitting function for an invariant mass plot will thus be:

$$f_{\text{total}}(x) = f_{\text{Gauss}}(x) + f_{\text{thresh}}(x) = \frac{p_2 e^{\frac{-(x-p_0)^2}{2p_1^2}}}{\sqrt{2\pi}p_1} + p_3(x - m_\pi)^{p_4}.$$

The standard fitting range used for this study is $[0.14, 0.165]$ GeV/c^2. A macro will determine the fitting parameters and will extract the necessary parameter values. The macro works as follows. First the background function is fitted, but not in the peak region; the background is plotted in the region 3σ away from the peak. The background parameters are thus completely determined. Next, the peak function is determined and the fitting parameters obtained. The total function f_{total} is then plotted.
The choice of background function effects the yield, because the Gaussian is fitted on top of the background. In the search for systematic error, another background function is studied:

$$f_{\text{exp}}(x) = p_3\sqrt{(x - m_\pi)}\exp(p_4(x - m_\pi)),$$

which is an exponential convoluted with a threshold function. Another source of systematic error is the fitting range used. The background function and thus the signal function will be different depending on the range, because other datapoints are (or are not) taken into account. In the systematic error estimation the fitting range will thus be varied, leading to different fitting functions.
Lastly, a PID is applied. This has a positive effect on the signal to background ratio, since the PID effects the background the most. The parameter which can be used to say more about how good a certain fit matches the data is the significance $\mathcal{S}$, defined as

$$\mathcal{S} = \frac{S}{\sqrt{S + B}},$$

with S the yield and B the background up to 3σ away from the peak. This parameter says something about how good the signal to background ratio is and will thus be important during our analysis.

5.1.2 Bin counting method

An alternative way to extract yield from the data is the bin counting method. The background function is fitted on the datapoints outside of the 3σ region around the peak. After this background function is determined, for each datapoint in the 3σ region the value of the background function is subtracted from the value of that datapoint. All these subtracted values are added to obtain the yield. If the yield did not depend on which of the two methods was used to calculate it, the ratio of the yield obtained by bin counting to the one obtained by fitting a function on the data would be one. The values of the two methods can thus be compared by looking at this ratio.

5.2 Dataset

This section covers the datasets that are used for this analysis. Two data samples were used: LHC13b and LHC13c, resulting in a total of about 120 million events.

5.2.1 Data sample LHC13b

System
p-Pb collisions at $\sqrt{s} = 5.02$ TeV, about 30 million events.

Runnumbers
$\{195344, 195346, 195351, 195389, 195390, 195391, 195478, 195479,$
$195480, 195481, 195482, 195483\}$

5.2.2 Data sample LHC13c

System
p-Pb collisions at 5.02 TeV, about 90 million events.

Runnumbers
$\{195529, 195531, 195532, 195566, 195567, 195568, 195592, 195593,$
$195596, 195633, 195635, 195644, 195673, 195675, 195677\}$

5.3 Results

5.3.1 Topological cuts

In this section I will go into detail about which topological cuts we use, what each one of them does and how we got to the final topological cuts for the first bin.

Topological cuts for p_{T} range $1-2$ GeV/c

In this section an analysis is done on the p_{T} range $[1,2]$ GeV/c. The goal is to find a set of topological cuts that maximize the significance and the signal over background ratio. This is done by trying various topological cut sets and identifying which of these cuts have a positive- and which have a negative effect. A summary of all used sets is presented in table 1. For each try,

#	D^0 m (GeV/c^2)	dca (cm)	p_{T} π,K (GeV/c)	$d_0^K \times d_0^\pi$ (cm^2)	$\lvert\cos\theta_{\mathrm{p}}XY\rvert$	NDL
1	0.32	0.04	0.8	-0.0002	0.99	2.7
2	0.032	0.04	0.8	-0.0002	0.97	2.7
3	0.032	0.035	0.7	-0.0002	0.97	4
4	0.032	0.035	0.5	-0.0002	0.97	4
5	0.032	0.035	0.6	-0.0002	0.97	4
6	0.032	0.035	0.7	-0.0002	0.97	3.5
7	0.032	0.035	0.7	-0.0002	0.99	0
8	0.032	0.035	0.7	-0.0002	0.99	3
9	0.032	0.035	0.6	-0.00022	0.99	0
10	0.032	0.035	0.6	-0.00024	0.99	1
11	0.032	0.035	0.6	-0.00024	0.99	3

Table 1: Summary of all studied topological cut sets for the p_{T} range $[1,2]$ GeV/c.

the values for d_0^K and d_0^π were 0.1 cm. The minimum- and maximum values for the transverse momentum of the soft pion were equal to 0.05 and 0.5 GeV/c, respectively. These sets are only a fraction of the variations tried, but they do represent the best cuts found and give a depiction of what the flow of the analysis was.
The invariant mass plot of the first set of cuts is depicted in figure 10. This is the starting set of cuts. The fitting macro tries to find a peak in the invariant mass region around 0.145 GeV/c^2, however the results are not good since the signal is cut too much and it is hidden in the background. The values for significance, signal, background and signal to background ratio are not to be considered relevant. A first attempt to improve on these results is set #2, for which the invariant mass plots for PID and without PID are showed in figure 11. This cut has a different value for the invariant mass of the D^0 and for the $\lvert\cos\theta_p XY\rvert$ (as can be seen from table 1). A much clearer peak is visible; especially in the PID case a clear peak is visible around 0.145 GeV/c^2. There is also a fluctuation visible in the invariant mass range $[151,158]$ MeV/c^2, in both PID and without PID. Applying the PID enlarges the signal to background ratio but also diminishes the significance of the fit. Set #2 was one of many tries done, but it seemed like there was something else needed to improve these plots.
The next logical step is trying to study the effect of applying a cut on the ITS for soft pion as well as D^0 decay daughters. The ITS is a multi-layered detector, the previous results all asked for a hit in one of the two innermost layers of the detector; it did not matter which one. As an alternative it is possible to require a hit in the first layer in one of the two cases (π_s or D^0 decay

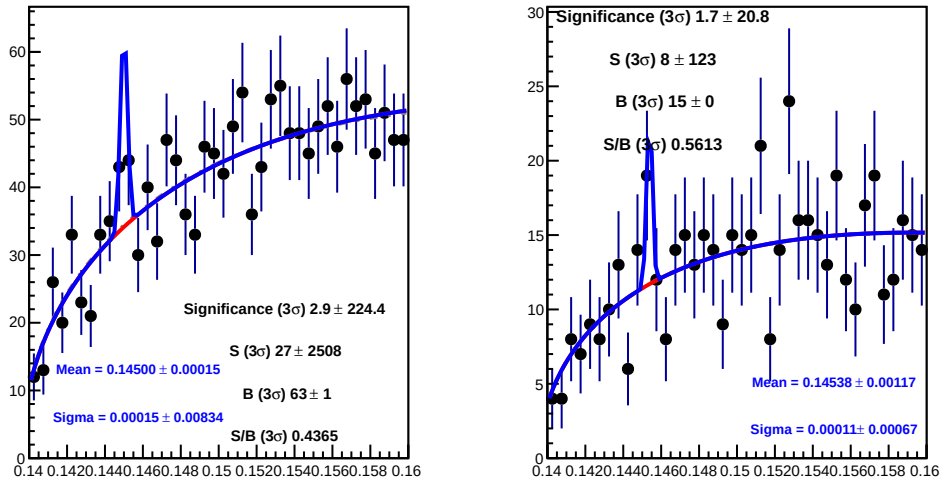

Figure 10: In the left panel the invariant mass distribution for set #1, without PID is shown. In the right panel the invariant mass distribution for set #1, with PID is shown. The invariant mass ΔM is in GeV/c^2 and the y-axis is in dN/dΔM.

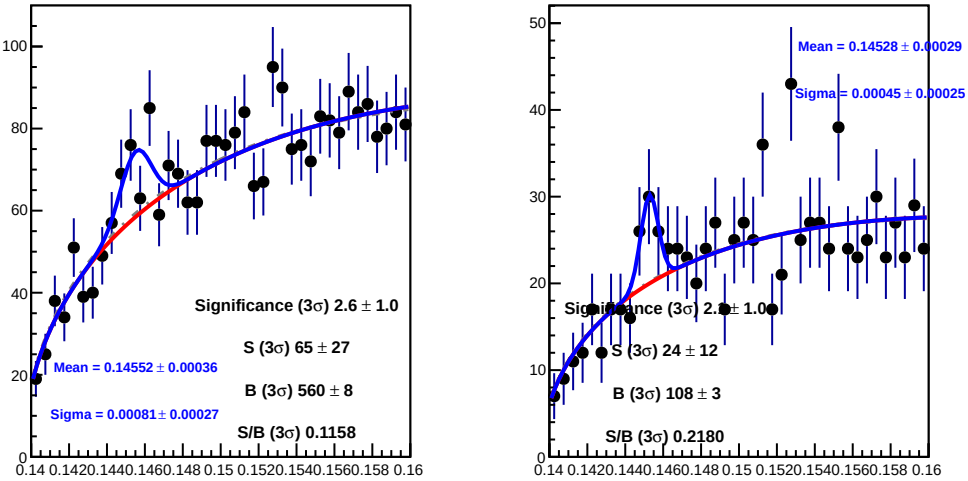

Figure 11: The left panel shows the invariant mass distribution for set #2, without PID. the right panel shows the invariant mass distribution for set #2, with PID. The invariant mass ΔM is in GeV/c^2 and the y-axis is in dN/dΔM.

daughters) or in both cases. The results from these four possibilities are depicted in figure 12. The first noticeable difference is that these plots boast a clearer peak; especially when a hit on

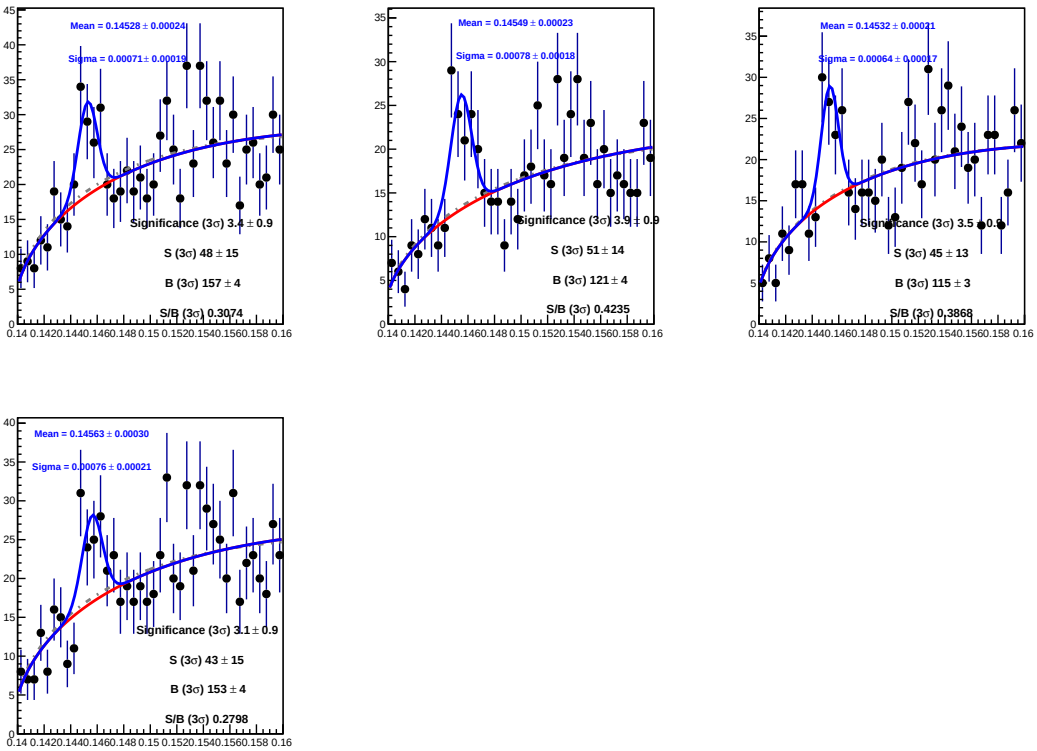

Figure 12: Invariant mass distributions for set #3, with PID. From left to right and top to bottom: hit on any of the layers in the two cases, hit on the first layer in the two cases, only a hit on the first layer for the D^0 decay daughters and finally only a hit on the first layer for the soft pion. The invariant mass ΔM is in GeV/c^2 and the y-axis is in dN/dΔM.

the first layer is required for both the D^0 decay daughters as well as the soft pion. For the sake of brevity, let us call these four sets of cuts A, B, C and D (from left to right and top to bottom, as in figure 12). Starting with A, this set gives a significance of 3.4, and a nicely visible peak. The signal to background ratio is about 0.30. The position the peak and its width are also within range. The B set is the best of the four results. It has the highest signal to background ratio, about 0.42, and a significance of 3.9. Set C and D are not as good as B, with a respective signal to background ratio of 0.39 and 0.28 and a significance of 3.5 and 3.1. This analysis showed us that using the ITS in a correct way gives better results and a clearer peak.
The question now is how to improve the fluctuations from 0.15 GeV/c^2 onwards. The results of the next trials are depicted in figure 13. Set #4, 5 and 6 all share the same parameters for the ITS, namely a hit is required in the first layer for both the D^0 daughters as the soft pion. This is done because this gave the best results in the previous set of cuts. With set #4 and 5 the p_T of both the kaon and the pion are varied, to see the effect that these parameters have. For the set of cuts #6, the normalized decay length has been varied. Set 4 and 5 look the most

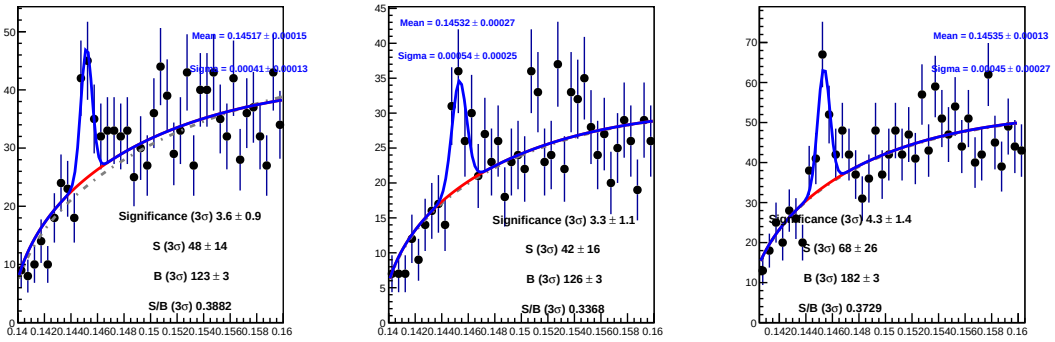

Figure 13: Invariant mass distributions for sets #4, 5, 6, with PID, arranged from left to right. The invariant mass ΔM is in GeV/c^2 and the y-axis is in dN/dΔM.

promising, but the width of the peak of #4 is not broad enough. Therefore, although set #6 has a smaller signal to background ratio (0.37 compared to 0.39) set #6 is picked as the best result. Its significance is also higher (4.3, compared to 3.6). Set #5 is clearly the lesser of the three sets in this case; it has a signal to background ratio of 0.34 and a significance of 3.3. Result #6 thus looks the most promising, the next set of cuts will try to tweak this result a little bit more to get the best set of cuts. Results #7 − 11 are the result of these trials. Again, a hit is required in the first layer of the ITS for both the D^0 daughters as the soft pion. The plots belonging to these sets are depicted in figure 14. Let us start by analysing set 7. The $|\cos\theta_p XY|$ has been changed from 0.97 to 0.99 and the norm decay length from 3.5 to 0. A small drop in significance is suffered with these cuts, but there is an increase visible in the signal over background ratio. The uncertainty on the signal is also slightly better: 14 instead of 18. Set #8 is almost the same as set #7, apart from a tighter cut on the norm decay length for #8: 3 instead of 0. The result is that the significance stays the same, but the signal over background ratio increases to 0.45. Tightening the norm decay length reduces the signal by 8% and the background by 18%. The next sets of cuts, #9 − 11, use a looser p_{T} cut for D^0 daughters (0.6 instead of 0.7). The norm decay length is varied, with values 0, 1 and 3, respectively. The tightening of the norm decay length has about the same effect as with set #8, although the looser p_{T} cut for K and π results in a lower significance and signal over background ratio. Thus set #6 and #8 look the most promising. Because of the higher significance for set #6, this set of cuts is chosen for p_{T} range $[1, 2]$ GeV/c.

Summary of topological cuts per p_{T} range

In the previous section (section 5.3.1) a study was done to find the best set of topological cuts for the first p_{T} bin, in the range $1 - 2$ GeV/c. The other p_{T} bins also have topological cuts, but the determination of these falls outside of the reach of this thesis. Table 2 is shown, which gives a summary of all topological cuts used per p_{T} bin.

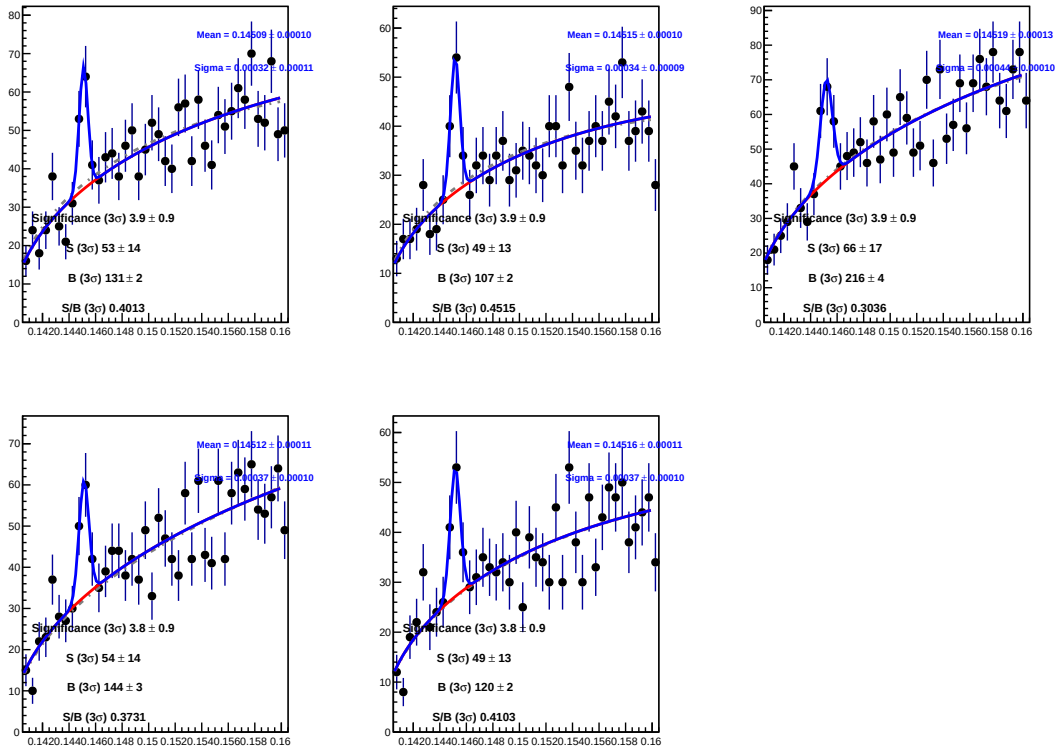

Figure 14: Invariant mass distributions for sets #7 – 11, with PID, arranged from left to right, top to bottom. The invariant mass ΔM is in GeV/c^2 and the y-axis is in dN/dΔM.

p_{T} (GeV/c)	[1, 2]	[2, 3]	[3, 4]	[4, 5]	[5, 6]	[6, 7]	[7, 8]	[8, 12]	[12, 16]	[16, 24]
D^0 inv m (GeV/c^2)	0.032	0.032	0.032	0.032	0.036	0.036	0.036	0.05	0.3	0.3
dca (cm)	0.035	0.035	0.03	0.04	0.05	0.05	0.055	0.06	0.06	0.1
$\cos\theta^*$	0.8	0.9	0.9	0.9	0.9	0.9	0.9	0.9	1	1
p_{T} pion (GeV/c)	0.7	0.6	0.5	0.5	0.5	0.5	0.5	0.5	0.	0.
p_{T} kaon (GeV/c)	0.7	0.6	0.5	0.5	0.5	0.5	0.5	0.5	0.	0.
d_0^K (cm)	0.1	0.1	0.1	0.1	0.1	0.1	0.1	0.1	0.1	0.1
d_0^π (cm)	0.1	0.1	0.1	0.1	0.1	0.1	0.1	0.1	0.1	0.1
$d_0^K \times d_0^\pi$ (cm^2)	-0.0002	-0.0002	-0.00015	-0.000015	-0.000015	0.00004	0.0001	0.0001	0.0002	0.001
$\cos\theta_{\mathrm{point}}$	0.94	0.92	0.92	0.92	0.8	0.7	0.7	0.7	0.	0.
π_s p_{T} min (GeV/c)	0.05	0.1	0.1	0.1	0.1	0.1	0.1	0.1	0.05	0.
π_s p_{T} max (GeV/c)	0.5	-	-	-	-	-	-	-	-	-
$\lvert\cos\theta_{\mathrm{point}}XY\rvert$	0.97	0.97	0.97	0.97	0.97	0.97	0.97	0.97	-1	-1
$NDLXY$	3.5	3.5	3.5	3.5	2	2	1	0	0	0

Table 2: Summary of topological cuts per p_{T} bin.

This table results in the plots depicted in figure 15, where the yield and significance resulting from this table can be seen.

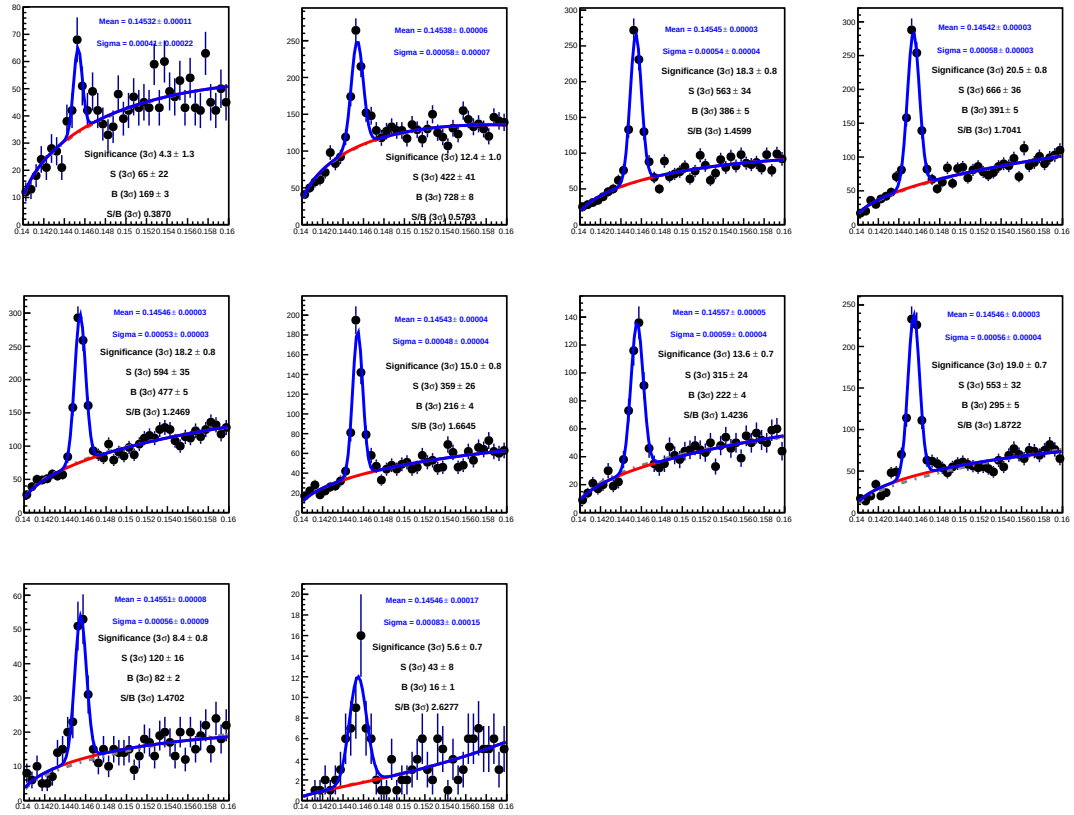

Figure 15: The final invariant mass distributions for all studied p_{T} bins. From left to right and top to bottom: 1-2, 2-3, 3-4, 4-5, 5-6, 6-7, 7-8, 8-12, 12-16, 16-24 GeV/c. The invariant mass ΔM is in GeV/c^2 and the y-axis is in dN/dΔM.

5.3.2 Systematic error calculation

Particle Identification

A check is done, to verify the workings of the particle identification (PID). The goal of the PID cut is to increase the signal over background ratio by decreasing the background; the signal should not be decreased too much. In figure 16 the ratio of the signal (before- and after applying the particle identification cut) and the same ratio for the background is depicted. The background

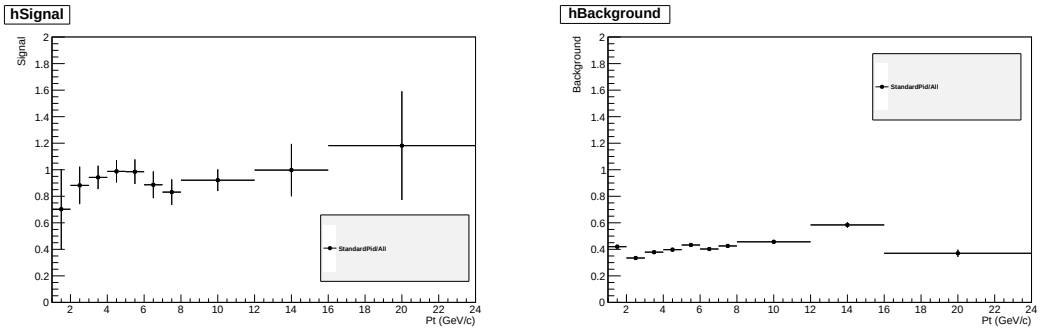

Figure 16: The left plot of the figure shows the ratio of the yield obtained with PID, divided by the yield obtained without PID. The right plot depicts this ratio, but for the background.

drops by a significant amount. Only 40% of the original background is left after applying the PID cut. The first nine p_{T} bins for the yield only drop by about 10%. In the last bin, with p_{T} range $[16, 24]$ GeV/c, the signal actually increases by about 20%. This can be explained by a larger sigma value for the PID case, than in the without PID case (0.00083 instead of 0.00072); this results in a larger yield.

Fitting parameters

One of the systematic error sources is the fit method for the background function. This is because the chosen fit range, as well as the chosen fit function has an influence on the obtained yield. As explained in section 5.1.1, the standard background function is a threshold function given by:

$$f_{\mathrm{thresh}}(x) = p_3(x - m_\pi)^{p_4}.$$

Another background function was fitted on the data to see how much this effects the yield. This function was a threshold function convoluted with an exponential, given by:

$$f_{\mathrm{exp}}(x) = p_3\sqrt{(x - m_\pi)}\exp(p_4(x - m_\pi)),$$

The ratio of the yield obtained by the f_{exp} divided by the yield obtained with f_{thresh} is shown in figure 17. Only for the first two bins is the absolute value of the difference between one and the calculated ratio bigger then 2%. The first bin has 40% more signal when the fit is done with f_{exp} than when the fit is done with f_{thresh}. For the second bin this number is 15%. Because of lower statistics, the first two- and the last two bins have a large uncertainty on the ratio values. The range on which the background function is fitted is also a source for systematic errors. The left and right ends of the fitting range for the standard background function (f_{thresh}) have been varied. Table 3 shows a summary of the changes done to the standard values of the fitting

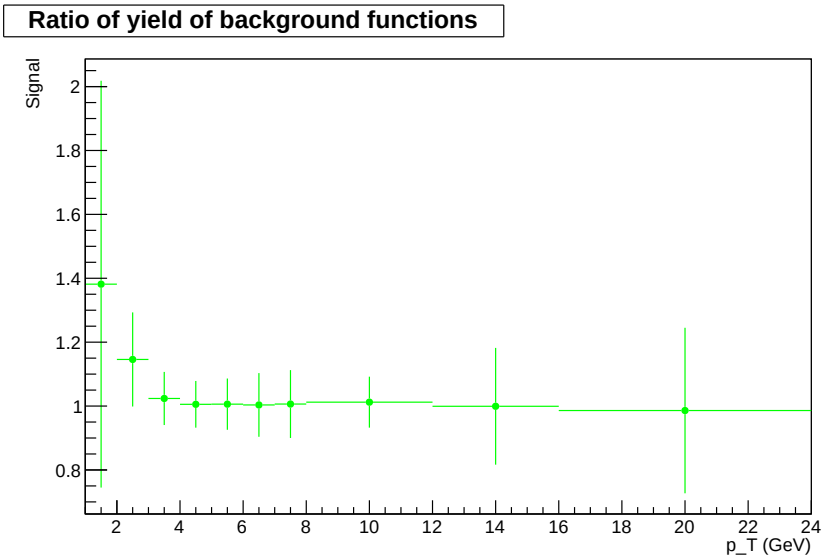

Figure 17: Ratio of yields obtained by the functions f_{exp} and f_{thresh}.

#	left range	right range	#	left range	right range
21	0.1400	0.1600	35	0.1395	0.1550
22	0.1405	0.1600	36	0.1395	0.1540
23	0.1410	0.1600	37	0.1395	0.1530
24	0.1415	0.1600	38	0.1395	0.1520
25	0.1420	0.1600	39	0.1395	0.1510
26	0.1425	0.1600	391	0.1395	0.1500
31	0.1395	0.1590	392	0.1395	0.1490
32	0.1395	0.1580	41	0.1395	0.1650
33	0.1395	0.1570	42	0.1395	0.1700
34	0.1395	0.1560	43	0.1395	0.1750

Table 3: Summary of parameter changes done to the fitting range. All values are in GeV/c^2.

parameters for each variation. Again, each yield is divided by the standard fitting function with standard fitting parameters. This ratio is showed per p_{T} bin in figure 18. The ratio of the yields when using different background functions, as shown in figure 17, is also depicted in this plot and given number 1. In the range $[3, 12]$ GeV/c are parameter changes results yield changes of less than 5%. In the p_{T} range from 12 to 24 GeV/c, a maximum difference of about 12% is seen. The second bin, apart from ratio 1, has a maximum difference of about 13%. In the first bin from 1 to 2 GeV/c, parameter change number 392 results in an increase of the signal with about 35%. This is quite a lot, but this could also be due to the fact that this cut is too close to the Gaussian of the signal (within 3σ). Ratio 392 also gives the biggest ratio difference in the last p_{T} bin, about 12%, while the other ratios are within 10%.

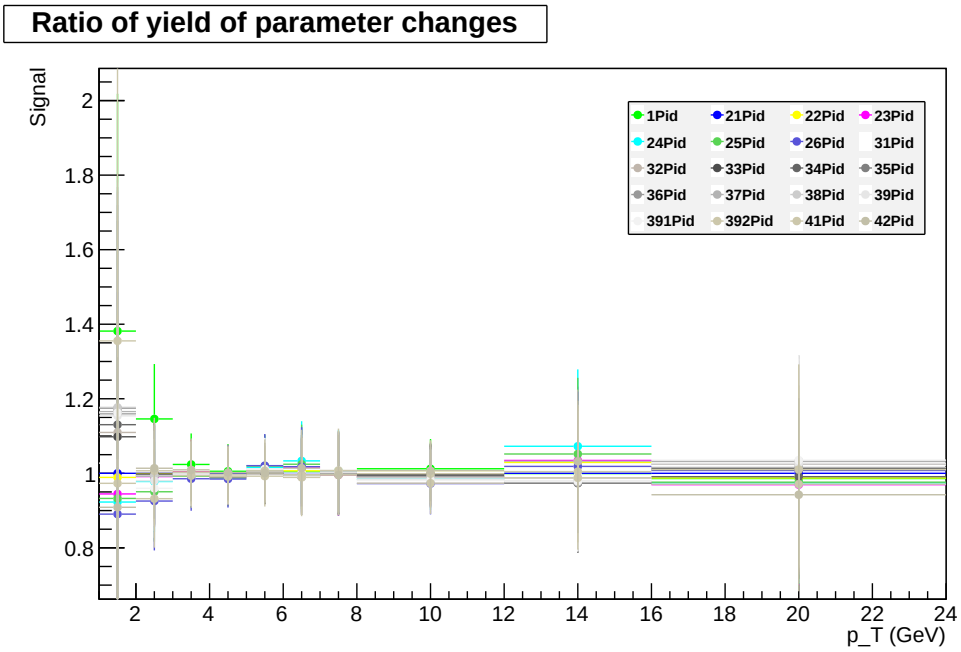

Figure 18: Ratio of yields obtained by the different variations of the fit range divided by the yield obtained when using the standard fit range. The ratio of the yields obtained when using different background functions is also depicted in this plot (# 1).

Bin counting method

In this section the effect of choosing the fitting method or bin counting method to obtain the yield is discussed. The bin counting is applied, with each bin 0.0015 GeV/c^2 in size. The yield is now calculated as described in section 5.1.2 and the ratio with the yield obtained using the standard fitting method is plotted in figure 19. The first p_{T} bin has a yield difference of about 13%. In the p_{T} range 2 to 6 GeV/c, the yield difference stays below 5%. From 6 to 7 GeV/c, a yield difference of about 8% is seen. From 7 to 8 GeV/c the yield difference is 5% and from 8 to 12 and 16 to 24 GeV/c it is about 5%. In the p_{T} range 12 to 16 GeV/c a yield difference of 17% is measured. Again, there are higher systematic errors at low and high p_{T} due to larger combinatorial background and less statistics, respectively.

Determination of the systematic uncertainties

In this section, the systematic error on the yield extraction is calculated per p_{T} bin. This is done with the results from sections 5.3.2 and 5.3.2. The following method is used to calculate the systematic error in a particular p_{T} bin. First, the maximum values of the yield difference are computed for each separate systematic error source (fitting parameters and bin counting). Next, the maximum of these two percentages is taken as an estimate for the systematic error in that p_{T} bin. The results of this calculation are shown in table 4. The usage of f_{exp} as a variation on the background function worsens the systematic error of the first two bins considerably. For the next six bins the systematic error stays around 5%. Bin $[12, 16]$ GeV/c has a big contribution to the

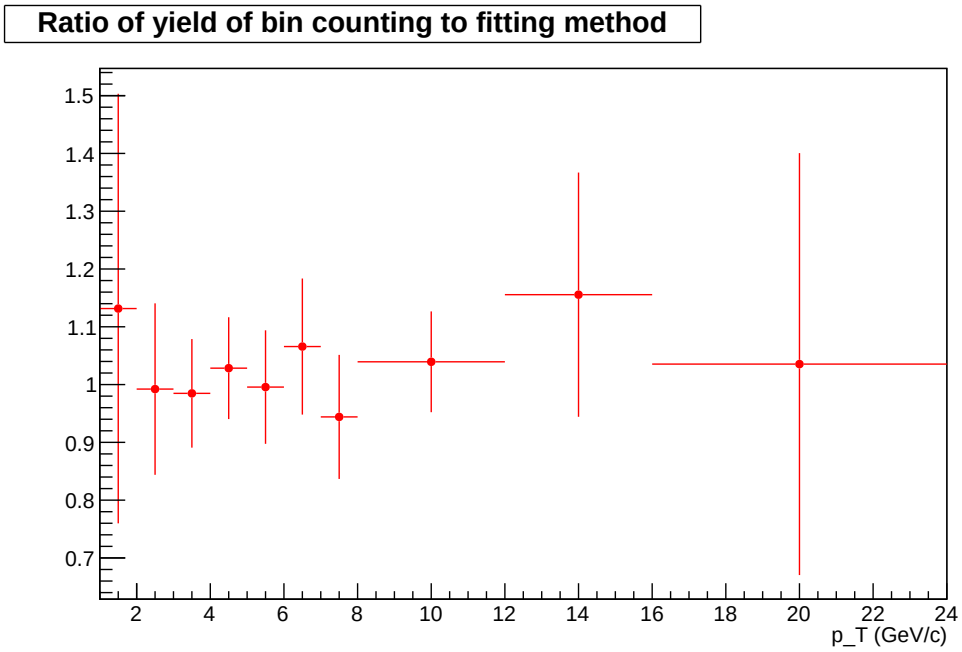

Figure 19: Yield obtained by bin counting method divided by yield obtained using fitting method with standard fit parameters. The mass range used for bin counting is 0.0015 GeV/c^2.

p_{T} bin (GeV/c)	Fitting parameters	Bin counting	Systematic error
1-2	38%	13%	38%
2-3	15%	1%	15%
3-4	3%	2%	3%
4-5	2%	4%	4%
5-6	2%	1%	2%
6-7	4%	8%	8%
7-8	1%	5%	5%
8-12	2%	5%	5%
12-16	10%	17%	17%
16-24	4%	5%	5%

Table 4: For each p_{T} bin the maximum ratio of variation of the standard fitting method by the standard method is given for the fitting parameters as well as when using the bin counting method. The final estimate for the systematic error on the yield extraction is then given in the final column.

systematic error from the bin counting method. In the p_{T} range 16 to 24 GeV/c the systematic error stays relatively small (especially for high p_{T}) with a systematic error of 5%.

5.4 Discussion

The research goal of this section was the extraction of the yield of charged D^* mesons in p-Pb collisions. After an explanation of the fitting method used to obtain the fit, topological cuts were searched to increase the yield and lower the background. This was done in the first p_T bin, from $1-2$ GeV/c. The results were better than the one the analysis started with and after searching around the best set of cuts found, it was believed that a local maximum for the significance in the phase space of topological cut parameters was found. One of the problems when using the iterative process that was used in this thesis is that all parameters depend on each other. The method used changes one parameter, looks for a maximum and then switches to another parameter where the process is repeated. In this way a local maximum for the significance is always reached, but starting with a different parameter will most likely result in a different local maximum and thus a different set of cuts. The question thus remains if the optimal cuts obtained in this work are in fact the best possible set of cuts. The only way to check this is using multidimensional optimization method, where with the help of a computer all parameters are changed at the same time. This makes sure that the global maximum of the significance in the phase space of topological cut parameters is reached. This however falls outside of the reach of this bachelor thesis.
After obtaining the 'optimal' set of cuts for the first bin a summary was given of the topological cuts for the other p_T bins. Next, a systematic error analysis on the yield extraction was done, cumulating in table 4 which gives a summary of the systematic error per p_T bin. A few bins can be discussed a bit further, namely 1-2, 2-3 and 16-24 GeV/c. In figure 18, it is clear to see where bin $1-2$ GeV/c gets its relatively large systematic error from. First there is the alternative background function, f_{exp}, which did not agree with the standard fit function on the yield; a difference of 38% was measured. This is largely due to the large combinatorial background for this first bin. The other source is parameter change 392, which sets the right end of the fitting range to close to the peak of the signal. This results in a big difference in the obtained yield. In the second bin, from 2-3 GeV/c again the biggest contributor to the systematic error is the variation of the background fitting function. Again this could be due to a large combinatorial background. The question is whether f_{expo} really describes the background that well.

6 $e - D^{*+}$ azimuthal correlations in 7 TeV proton-proton collisions

6.1 Analysis Method

6.1.1 Electron Identification

In this subsection, the method applied to select electrons will be discussed. The identification of electrons is done using the TPC and EMCal detector. The TPC uses ionisation energy loss and to reach high p_{T} and better purity, the EMCal is used. The EMCal detector measures the energy deposited in the detector material. Reconstructed clusters in the EMCal detector are geometrically matched to tracks. The TPC and ITS detectors provide the momentum information. Figure 20 show the dE/dx versus momentum p for different tracks in proton-proton collisions at $\sqrt{s} = 7$ TeV. Tracks are selected in the analysis if they have a $\sigma_{TPC-dE/dx} \in [-1, 3]$. Due to their

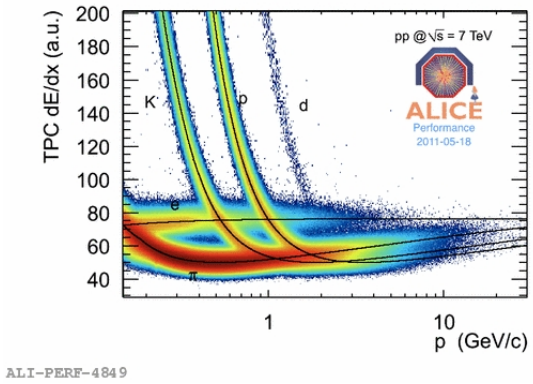

Figure 20: dE/dx versus p for tracks coming from pp collisions at $\sqrt{s} = 7$ TeV. Different particles are characterized by their respective bands. At high p these bands converge. [17]

low mass and the fact that electrons deposit their total energy in the EMCal, electrons have an E/p ratio of approximately one (see figure 21 for an example in a specific p_{T} range). Thus tracks with E/p ratio between 0.8 and 1.2 are selected as electrons. Now, the tracks which satisfy the range for $\sigma_{TPC-dE/dx}$ and the value we have for E and p from the respective detectors can be used to identify electrons. In figure 22, the electron area for E/p and $\sigma_{TPC-dE/dx}$ is rather well bounded for a particular example.

6.1.2 Heavy flavour azimuthal correlation

This is a general section, describing correlations between heavy flavour electrons and hadrons. Azimuthal angular correlation between heavy flavour electrons (from charm and beauty) and different hadron species can be used to distinguish and separate charm and beauty. In ALICE, $\Delta\phi(e_{HF}, h)$ are used to calculate relative beauty fractions; the hadrons h used are charged. By applying PID on hadrons or selecting heavy flavour hadrons, more information on the fragmentation of c and b can be obtained. Figure 23 gives a schematic overview of the fragmentation of $c\bar{c}$ and $b\bar{b}$ pairs. The $\Delta\phi$ correlations are used to distinguish between the two, so a specific hadron which gives a different distribution depending on like- or unlike sign should be used. In this paper, the azimuthal correlation between electrons and D^{*+} mesons is studied. How this specific correlation is done, is described in the following section.

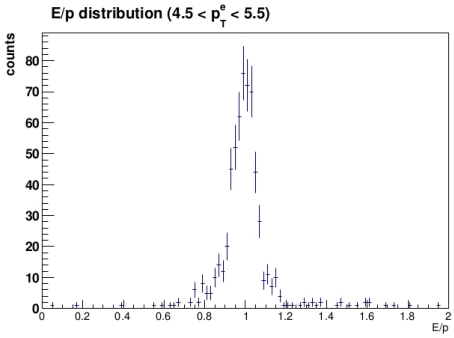

Figure 21: E/p for electrons in p_{T} range 4.5 - 5.5 GeV/c for pp collisions at $\sqrt{s} = 2.76$ TeV. [17]

6.1.3 $\mathbf{e-D^{*+}}$ correlation

This section explains how to study the like- and unlike-sign correlation distribution for heavy flavour- and non-heavy flavour electrons with charged D* mesons. This is done using a Monte Carlo generated 7 TeV proton-proton Monte Carlo sample. The selection of electrons for heavy flavour correlation is done as follows. First the electron is selected using the TPC and EMCal. Next, the mother of the electron is looked at. If it is a B meson, then that electron comes from a b quark, is it a D meson then the analysis has to go one step further. In this case it is checked if the D meson comes from a B, because then the trigger electron also comes from a b quark. If the D meson did not come from a B meson, the trigger electron came from a c quark. Next, the method of finding the D* in that event is discussed.
Next, in that particular stack a selection is made of pions, coming from charged D* decays. This π should have a p_{T} value greater than 0.3 GeV/c. Once such a π is found the next step takes place. The mother of the pion is looked at to determine whether it is a D^0 meson or not. If this is the case, the D^0 is required to have both a K and a π as daughters, and a D* as mother particle. Once this D* is found, the last step is to determine whether it came from a b or c quark. Thus the point in the analysis is now reached that we have an electron coming from a c or b quark and a D* coming from a c or b quark in the same event. The next step is to do a sign comparison. The sign of the electron and the pion (decay daughter of the charged D*) is compared. This pion will have the same sign as the D*, due to the way the D* decays. If the electron and pion share the same charge sign, they are of like sign. If they are not, they are of unlike sign. Now the like- and unlike sign case are looked at separately, and in each case the azimuthal angle that the electron makes with the D* is noted. For the Monte Carlo data, an enhanced sample was used in first instance. This enhanced sample uses a p_{T} cut for the electron: the electron should have a p_{T} higher then 5 GeV/c. The electron thus has a relatively large energy and thus has a higher chance of coming from a heavy flavour pair. The result is a larger fraction of $c\bar{c}$ and $b\bar{b}$ pairs per event. Of course, this thesis deals with finding a way to distinguish $c\bar{c}$ events from $b\bar{b}$ events. Thus a subresult of this analysis, which shows that the $\Delta\phi$(e,D*) correlation can be used in such a way, is needed. However, in order to compare $b\bar{b}$ and $c\bar{c}$, we should scale both plots down since the number of $c\bar{c}$ and $b\bar{b}$ events are not the same in real physical reactions. Both have a certain chance of happening. One way to compare them is to look at these chances and scale one of the two plots down, so they can be compared. Another way of doing this, which achieves

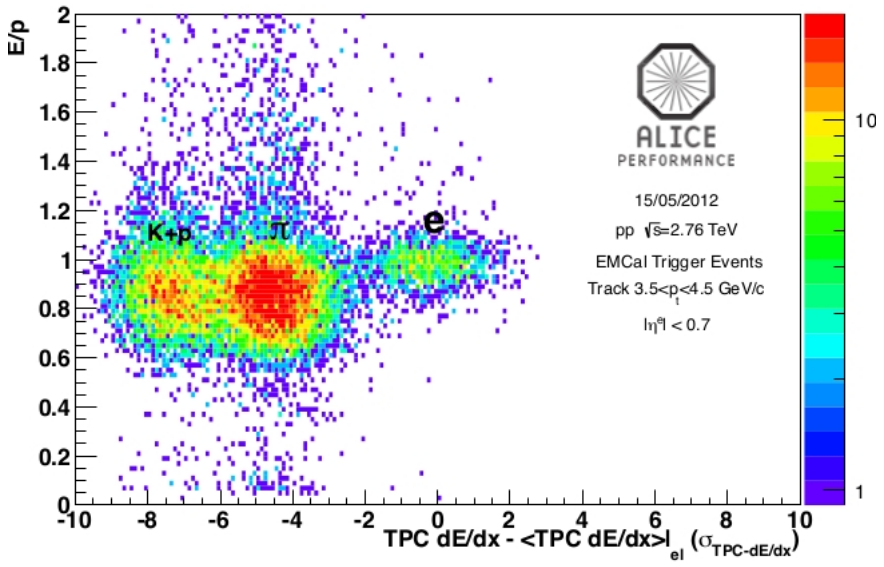

Figure 22: E/p versus $\sigma_{TPC-dE/dx}$ for pp collisions at $\sqrt{s} = 2.76$ TeV. A clear separation between kaons, protons, pions and electrons can be made. [17]

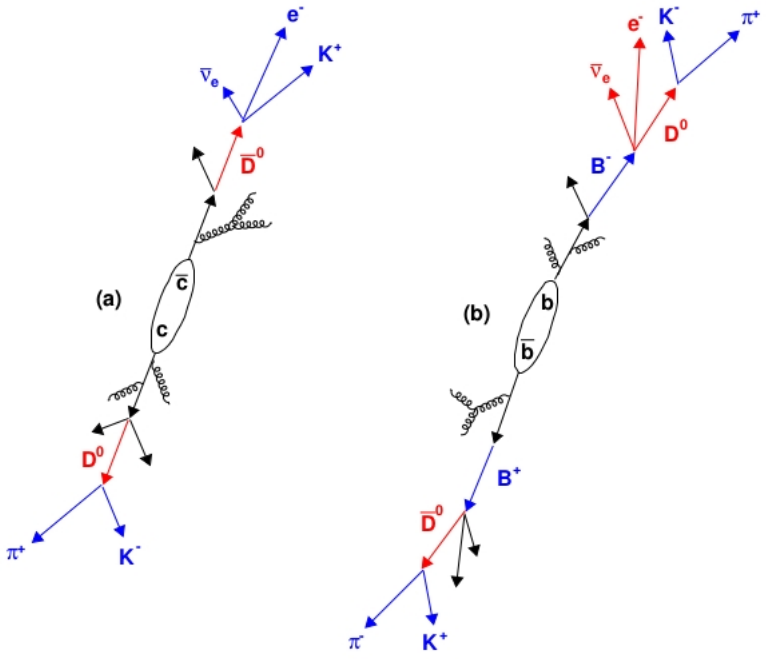

Figure 23: Schematic overview of the fragmentation of (a) $c\bar{c}$ and (b) $b\bar{b}$ pairs. [18]

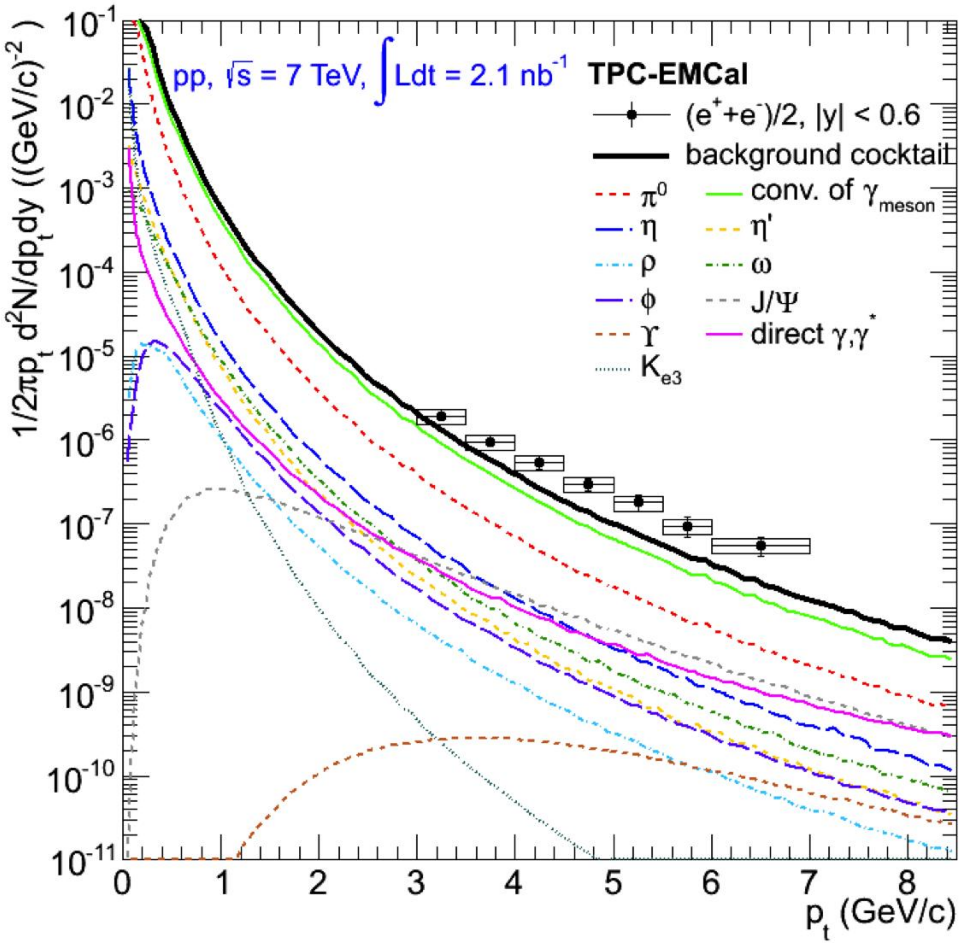

Figure 24: Overview of origin of non-heavy flavour electrons and their respective contributions. [17]

the same thing, is by looking at a minimum bias sample. The minimum bias sample is different from the enhanced sample in that the enhanced sample has heavy flavour in every event. This gives higher statistics and reaches higher p_{T}. The number of $c\bar{c}$ and $b\bar{b}$ pairs are simulated to be the same as real physical results obtained via experiment. The minimum bias sample will be used to look at heavy-flavour electrons.
Non-heavy flavour electrons give insights into the background signal. These are electrons originating mostly from π^0, η and γ. All contributions are depicted in figure 24. Non-heavy flavour electrons are correlated in the same way as their heavy flavour counterparts, in the sense that for non-heavy flavour electrons like- and unlike-sign correlations on different electron p_{T} ranges are done.

6.2 Dataset

An enhanced- and a Minimum Bias (MB) Monte Carlo sample was studied. The specifics of both MC samples are given below.

6.2.1 Enhanced Monte Carlo sample

Data sample
LHC12d2

Event generator
PYTHIA

Description
7 TeV, heavy flavour enhanced, 6 million events.

System
pp at $\sqrt{s} = 7$ TeV

Runlist
{156889, 156891, 157275, 157277, 157564, 157734, 158086, 158285, 158287, 158304, 158492, 158516, 158520, 159538, 159580, 159582}

6.2.2 Minimum Bias Monte Carlo sample

Data sample
LHC10f6a

Event generator
PYTHIA

Description
7 TeV, Minimum Bias, 150 million events.

System
pp at $\sqrt{s} = 7$ TeV

Runlist
{126422, 126424, 126425, 126432, 126437, 126090, 126097, 126158, 126160, 126167, 126073, 126078, 126081, 126082, 126088, 126168, 126283, 126284, 126285, 126350, 126351, 126352, 126359, 126403, 126404, 126405, 126406, 126407, 126408, 126409}

6.3 Results

6.3.1 Enhanced Monte Carlo sample

In this section, the correlation is shown between heavy flavour (HF) and non-heavy flavour (NHF) electrons with D* in an enhanced sample. The sample used is described in section 6.2.1. The sample is enhanced for heavy flavour electrons. For this analysis a clear correlation is thus expected, because of higher statistics. The correction for the ratio of beauty versus charm quarks will be done later, since this is not represented well with this particular sample. As discussed, this is done by using the minimum bias sample. For the enhanced heavy flavour sample, two different results are shown. In the first, the MonteCarlo track is not a physical primary, in the second it is. By asking that the track is a physical primary, it is made sure that the electron is coming from the collision and not from detector effects. When we ask that the track is a physical primary, we call this 'without detector effects'.

Heavy Flavour with detector effects

In this section, heavy flavour electrons are discussed. These electrons come from the initial physical processes and from interaction with the detector. The results are shown in section A.1 of the appendix. Figures 33- 36 show the azimuthal angular correlation distribution for electrons coming from $b-$, $c-$, $b-$ and c quarks and D* from $b-$, $c-$, $c-$ and b quarks, respectively. *The following notation is used: if it is written that a reaction stems from $[p,q]$ then this means that the electron comes from a p particle and that the D^* comes from a q particle.* Firstly, the $[b,b]$ reactions are shown in figure 33. There is an away-side peak in the like sign case, and a near-side peak in the unlike sign case. For higher p_{T} (above 13 GeV/c) it is often difficult to say anything because of low statistics. Next, the results for $[c,c]$ are summarized in figure 34. In the like sign case, there is a slight peak at the away-side but this peak is not strong. Again, for high p_{T} there cannot be made any conclusions. For the unlike sign case, a clear peak at the away side and a small peak at near side can be distinguished. Thirdly, the $[b,c]$ case is discussed in figure 35. For the like-sign case not much can be said above 11 GeV/c because of low statistics. For low p_{T} the $\Delta\phi$ distributions look relatively flat. In the unlike-sign case there is a clear peak present at near-side. There are slightly better statistics for the unlike-sign case, there is a relatively good signal for the distribution until 13 Gev/c. Lastly, the $[c,b]$ case is discussed in figure 36. There is a flat distribution in both sign cases and both have poor statistics above 7 Gev/c. Figure 25 shows all like-sign plots, but p_{T} integrated from $1-19$ GeV/c. There is a clear away-side peak for the $[b,b]$ case, but all the others have relatively flat distributions. There are small peaks for $[b,c]$ and $[c,c]$ but these are not significant. Next, the p_{T} integrated case for unlike-sign is discussed. The results are shown in figure 26. For the $[b,b]$ case, there is a peak at near-side, just as for the $[b,c]$ case. Thirdly, the distribution for $[c,b]$ is flat. The distribution for $[c,c]$ has a small peak at the near-side and a larger peak at the away-side. The away-side peak can be explained by the back-to-back contribution from the $c\bar{c}$ pair. The contributions to the near-side peak will be investigated further in the Discussion of this section.

Heavy Flavour without detector effects

In this section the same data as in the previous section is analysed, but without the detector effects. This is done by putting a flag in the code, which is called 'IsPhysicalPrimary'. Setting this flag makes sure that electrons do not come from reactions with the detector, they originate purely from the initial collision. The same distributions as in the previous section are thus expected, although with less background signal. The results per p_{T} bin are summarized in appendix A.2, in figures 37- 40. Slightly less statistics than in the previous section are the result of setting

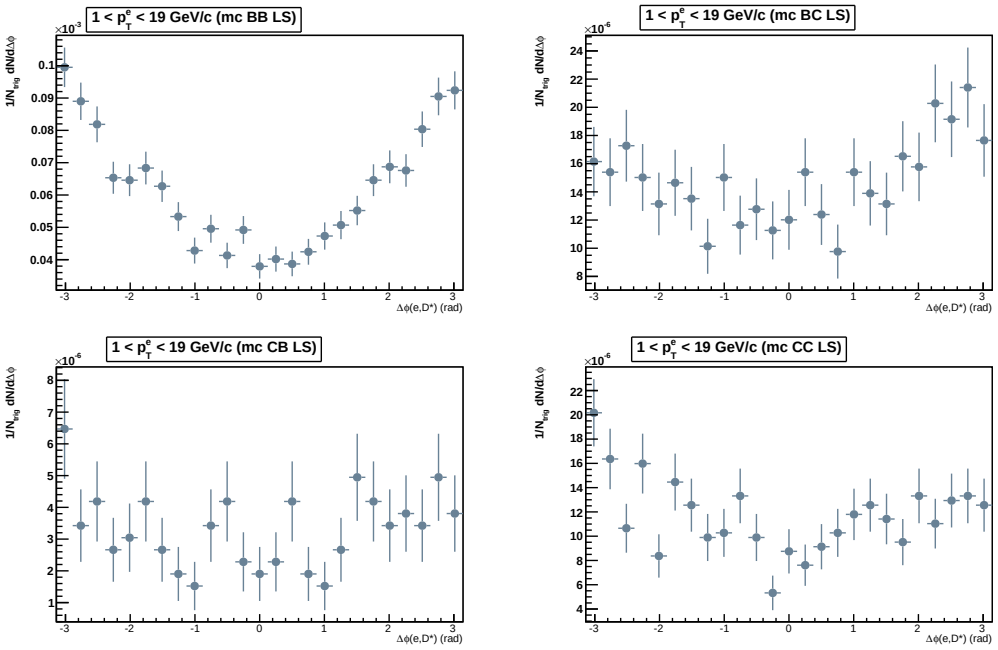

Figure 25: $[b,b],[c,c],[c,b],[b,c]$ reactions in their respective like-sign cases, p_{T} integrated from $1-19$ GeV/c.

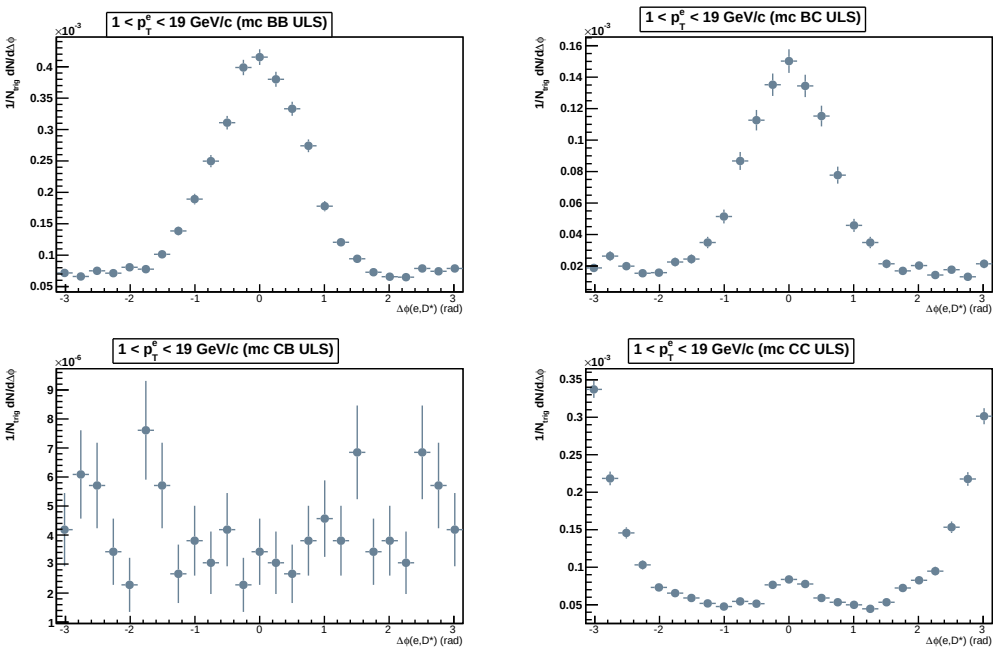

Figure 26: $[b,b],[c,c],[c,b],[b,c]$ reactions in their respective unlike-sign cases, p_{T} integrated from $1-19$ GeV/c.

the 'IsPhysicalPrimary' flag. This is because decays and reactions with the detector volume are missing. Also, the distributions look the same. The peaks are all in the same position, as was expected. This is because eliminating detector effects only takes away random data points. These points are not biased to have a certain $\Delta\phi$ value. Thus the distributions look almost the same as in the previous section. This check gives an idea of how the correlation looks like in a Monte Carlo dataset with only particles originating from the initial proton-proton collision and are therefore interesting. Next, the like- and unlike-sign correlations, fully integrated over the entire p_{T} spectrum are shown in figure 27. After comparison, the results with detector effects agree to the ones without, as expected.

Non-Heavy Flavour with detector effects

In this section, non-heavy flavour electrons are studied. This means electrons coming from γ-, π^0- and η particles, respectively. When real data is used for correlations, the inclusive electrons contains both heavy flavour and non-heavy flavour. The study of non-heavy flavour electrons gives an estimate for the background signal. We use the same data sample as with the heavy flavour study we did. The results are depicted in appendix A.3, in figures 41- 44. Figure 41 shows a distribution where electrons are coming from γ and D^* from B meson decays. There are two clear peaks: one on the near-side and one on the away-side. This holds for both the like-sign as the unlike-sign case. At higher p_{T} (above 11 GeV/c) the statistics do not allow for the identification of any sort of distribution. Figure 42 shows the results for electrons coming from γ and D^* from c quarks. The same distributions as in the $[\gamma, b]$ case are visible. The results after p_{T} integration are shown in figure 28. All four distributions look the same: one peak at near-side and one at away-side. Next, electrons coming from π^0 and η are discussed. Both origins of the electrons are looked at together and the results are shown in figures 43- 44. Because of low statistics there are not many conclusions possible to make, but in both the like-sign and unlike-sign cases there is a slight peak at near- and away-side visible, just like it was the case with $[\gamma, b]$ and $[\gamma, c]$. Almost all particles are in the $1-3$ GeV/c range, so this is what the p_{T} integrated spectrum looks like.

Non-Heavy Flavour without detector effects

In this section, the non-heavy flavour case for the same enhanced dataset is studied. This time, electrons not originating from conversions and secondary weak decays are selected. Again, as was the case with heavy flavour, the same results as in the previous section are expected, only this time with lower statistics. This is because only background is subtracted by applying this selection. Of course, without taking detector effects into account, we know that there will be no electrons coming from γ any more. γ particles originate from conversions with the detector volume and decays and are thus filtered by this flag. So, only electrons coming from π^0 and η are correlated with D^* in this section. Results are shown in figure 45 in appendix A.4. This time only the p_{T} integrated case are shown, since the distribution of the signal over the p_{T} spectrum is the same as last time. Again, there are peaks visible at near- and away-side, but these are not very clear probably because of statistics. The same distribution are seen as in the case when detector effects were taken into account.

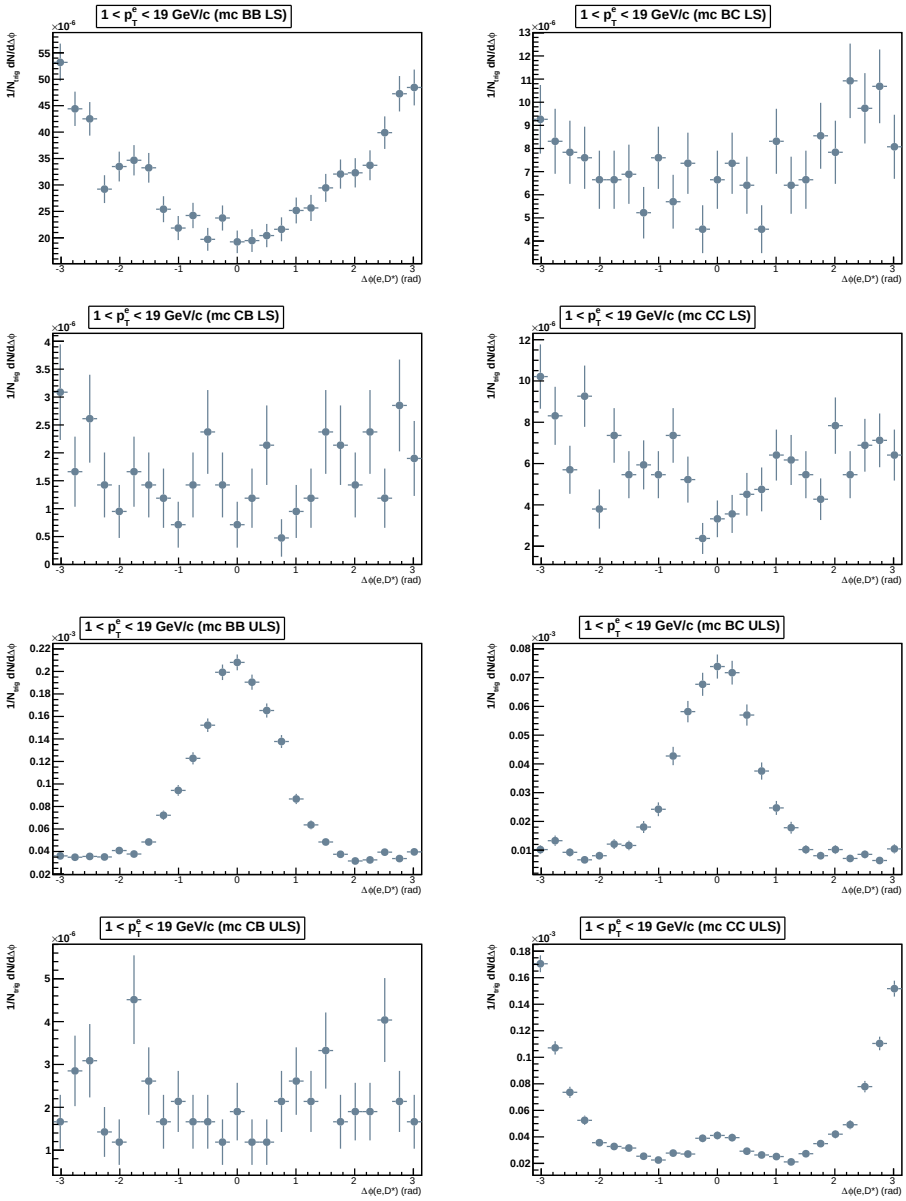

Figure 27: Upper four panels show the like-sign $e-\mathrm{D}^{*+}$ correlation for enhanced heavy flavour, p_{T} integrated from 1-19 GeV/c. Lower four panels show the unlike-sign $e-\mathrm{D}^{*+}$ correlation for enhanced heavy flavour, p_{T} integrated from 1-19 GeV/c.

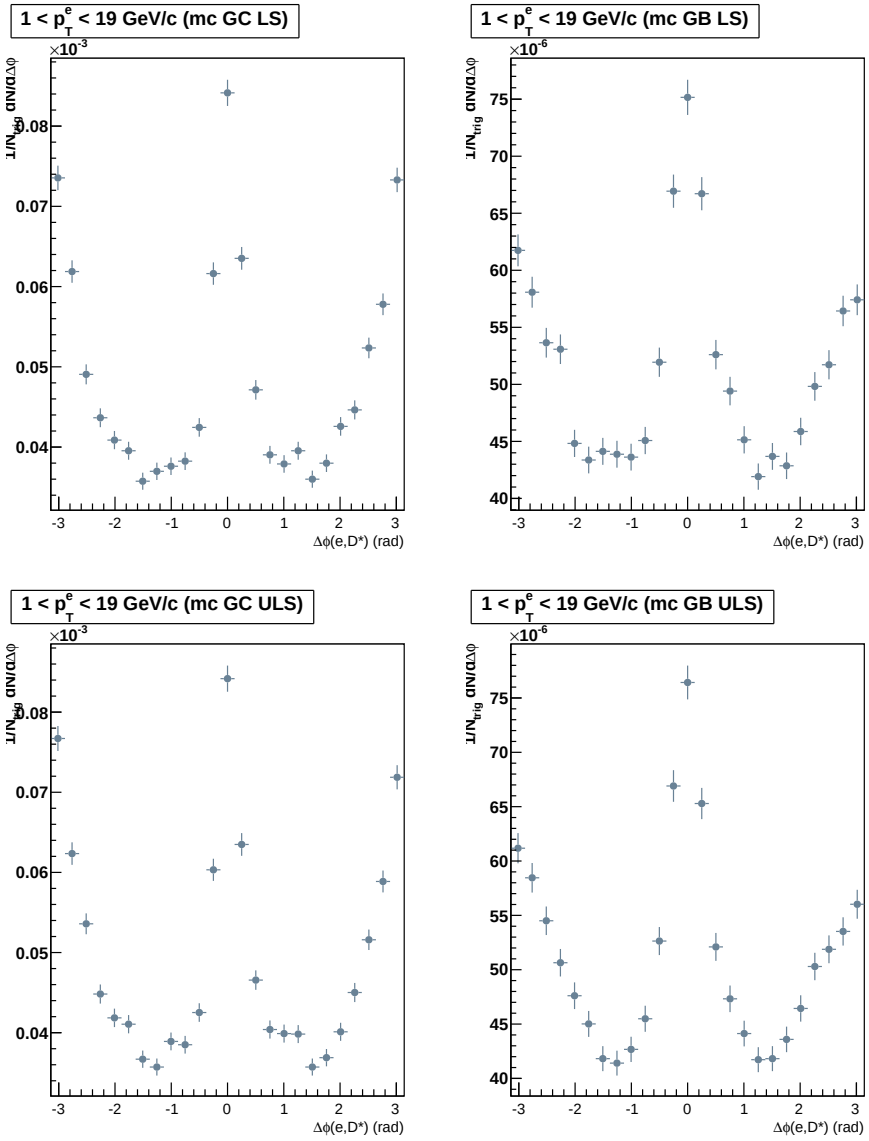

Figure 28: The upper two panels show the like-sign $e-\mathrm{D}^*$ correlation for non-heavy flavour γ, p_T integrated over the full spectrum. The lower four panels show the unlike-sign $e-\mathrm{D}^*$ correlation for non-heavy flavour γ, p_T integrated over the full spectrum.

6.3.2 Minimum Bias Monte Carlo sample

In this section, the correlation distribution is shown between heavy flavour electrons and D* for the minimum bias data sample. Electrons from Pythia only are selected. An $|\eta| < 1$ bound is imposed on the electron (denoted as η_e), so as to mimic the detector. The results are shown in appendix B.1, in figure 46. That the statistics overall are quite poor is clearly visible. Especially in the $[b, c]$ and $[c, b]$ cases. The $\Delta\phi$ distributions cannot be determined in these two cases. The unlike-sign case for electron from c and D* from c has a peak at away side. Such a trend is also visible in the $[b, b]$ like-sign case. The $[c, c]$ like-sign and $[b, b]$ unlike-sign cases are not clear enough to give a conclusive answer. It is clear that more statistics are needed in order to improve on this study in the minimum bias case. The interpretation of these results are left to the discussion, where the possibility of differentiating between $[b, b]$ and $[c, c]$ using $\Delta\phi$(e,D*) correlations will be discussed.

6.3.3 Process types

In this section, different process types for the electrons are looked at, namely gluon splitting, flavour excitation and pair creation. For the analysis, the origin of the electrons is noted, which could be charm or beauty. The origin of the D* mesons is not looked at. The final results are shown in these sections, the others are in appendices C.1- C.3.

Gluon Splitting

In this section electrons that come from the process type gluon splitting are discussed. This type is characterized by $gg \to g(\to Q\bar{Q})g$. Which means that two gluons react into forming another gluon pair with a quark anti-quark pair. The studied electrons come from charm or beauty quarks. The $\Delta\phi$ distribution between the electron and the D* meson is analysed, in low- (1-11 GeV/c) and high (11-19 GeV/c) p_{T}. The analysis starts with the low p_{T} region for the like-sign and unlike-sign case. The results are presented in figure 47. For the like-sign case, electrons descending from b quarks have a flat $\Delta\phi$ distribution. For electrons originating from c quarks there is a sharp peak around zero, with no away-side peaks. For the unlike-sign case, electrons coming from b quarks all have a broad peak in the middle, with a small dip for the 1-3 GeV/c p_{T} case. Electrons coming from c quarks have a small peak at near-side and also an away-side peak. In addition, the high p_{T} region for gluon splitting is discussed. Results for this case are shown in figure 48. For the like sign case, a peak for electrons coming from c quarks is visible, while electrons from b have a flat distribution. For the unlike sign case, there is a peak at near side for electrons originating from b quarks and a small peak at away side for electrons originating from c quarks.

Flavour Excitation

In this section, electrons that come from the process type flavour excitation are looked at. This type is defined by $gQ \to gQ$, which means that a quark and a gluon react and form a gluon and a quark, although with a different colour charge. Thus electrons are studied coming from this reaction, where the electrons are descendants of charm or beauty quarks. Again a low- (1-11 GeV/c) and high (11-19 GeV/c) p_{T} case will be distinguished. For the low p_{T} region the results are shown in figure 49. In the like-sign case, a clear peak at zero for electrons coming from charm quarks and a flat distribution for electrons coming from beauty is visible. In the unlike-sign case, electrons coming from charm quarks have a small peak at near-side and a peak at away-side. Electrons coming from beauty quarks show a broad peak at near-side. Next, the high p_{T} case

is shown in figure 50. In the like-sign case there is still a peak at near-side for electrons coming from charm quarks. The distribution for electrons coming from beauty quarks is also still flat. In the like-sign case, the near-side peak is almost completely gone for the electrons coming from charm quarks and the away-side peak is less strong. For electrons coming from beauty quarks a strong peak at zero is visible.

Pair Creation

Next, the process type called pair creation is discussed, which is characterized by $gg \rightarrow Q\bar{Q}$, i.e. two gluons react into forming a quark-pair. Again, electrons coming from charm or beauty quarks and descending from a pair creation process are studied. Low- and high p_{T} cases are treated separately, in the same way as with the previous two process types. The $\Delta\phi$ distribution for electrons with D^* mesons are determined. The low p_{T} region is looked at first, the results are summarized in figure 51. For the like-sign case, a clear peak at zero for electrons from charm quarks is visible. For electrons coming from beauty quarks, there is a small, broad peak at the away-side. In the unlike-sign case, a strong, broad peak for electrons from beauty at near-side and a small, broad peak at the away-side is visible. For electrons coming from charm quarks, there is a small peak at near-side and a strong peak at away side. Next, the high p_{T} region is shown, for which the results are depicted in figure 52. For the like-sign case, a strong peak at near-side for electrons coming from charm quarks and a small away-side peak for electrons from beauty quarks is visible. In the unlike-sign case, there is a near-side peak for electrons coming from beauty quarks and a small away-side peak for electrons coming from charm quarks.

6.4 Discussion

The question that the study of azimuthal correlation of electron with a charged D* meson wants to answer is if this particular correlation can separate c and b signal. This was done using two data samples, namely an enhanced- and a minimum bias sample. For the first, a study was done on heavy flavour and non-heavy flavour electrons. The non-heavy flavour contribution is in fact our background and it is thus interesting to see how signal and background look in comparison to each other. Let us thus look at a joined distribution of both signal and background. This is the summation of figure 27 (where we have added like- and unlike-sign cases and all origin possibilities of the electron and D* ($[c,c],[c,b],[b,c],[b,b]$) and figure 45 (where we did the same thing, but for $[X,c]$ and $[X,b]$ with X either π^0 or η). Figure 29 depicts these summations. The error margins for the non-heavy flavour distributions are bigger because of lower statistics.

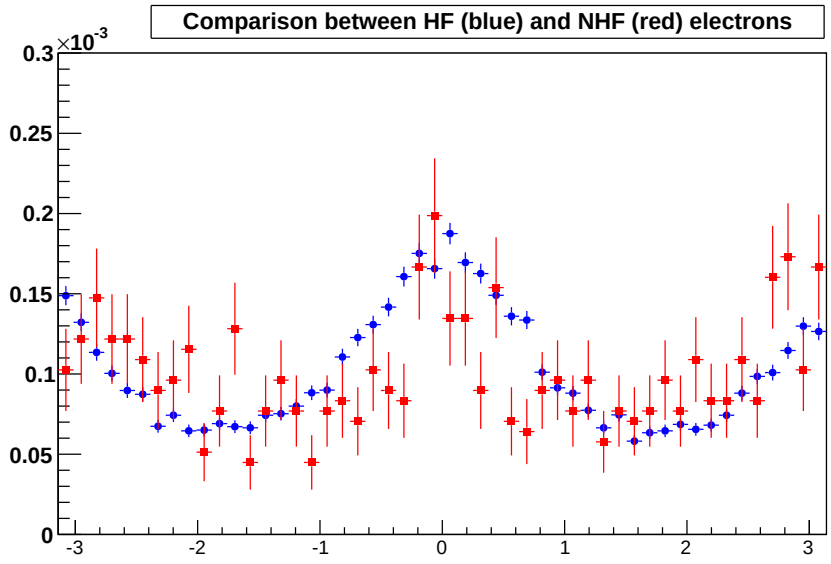

Figure 29: Plot of azimuthal correlation between electrons and charged D* mesons, where the electron is heavy flavour (blue) or non-heavy flavour (red). No charge sign cut is applied. Each distribution is scaled to the number of electrons. On the x-axis the $\Delta\phi$ in radians is depicted, while on the y-axis there is $\mathrm{d}N/\mathrm{d}\Delta\phi$ in rad^{-1}.

A sharper peak is visible on the near-side for the non-heavy flavour distribution than for the heavy flavour distribution which has a broader peak. On the away-side, the non-heavy flavour distribution is comparable with the heavy flavour distribution.
Next, let us look at the separation possibilities of c and b using the $\Delta\phi(e_{\mathrm{HF}},\mathrm{D}^*)$ correlation method. This is again a summation of figure 27, but this time only the separate like- and unlike-sign cases for $[c,c],[c,b],[b,c]$ and $[b,b]$ are added. In this way, four different distributions are obtained. These are depicted in figure 30. The left panel of the figure shows that $[b,b]$ has a peak at near-side and a small peak at the away-side, while $[c,c]$ has a small peak at near-side and a big peak at the away-side. If it weren't for these small peaks, this analysis method would already be able to separate c and b events. Unfortunately, there are peaks at the near- and away-side from both contributions. Thus, another cut has to be applied: a charge sign cut. Figure 31 shows the

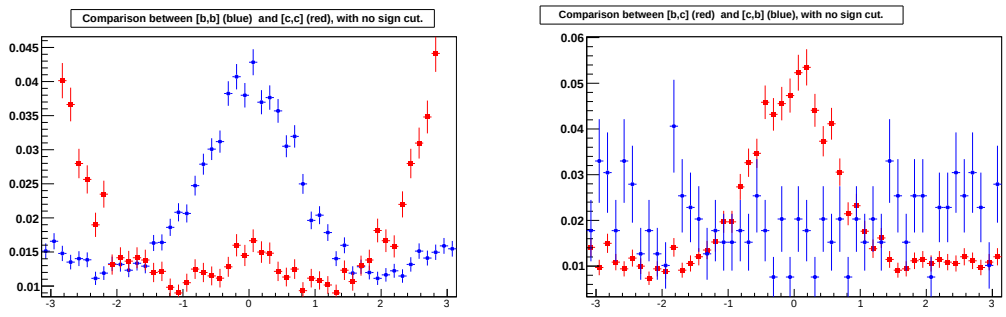

Figure 30: The left panel shows the $\Delta\phi$ distribution for $[b,b]$ and $[c,c]$, with no charge sign cut. The right panel shows this for $[c,b]$ and $[b,c]$. On the x-axis the $\Delta\phi$ in radians is depicted, while on the y-axis there is $\mathrm{d}N/\mathrm{d}\Delta\phi$ in rad^{-1}.

results of both the like-sign and the unlike-sign cut for $[c,c]$ and $[b,b]$. Again, the plots are scaled by their respective integrals over the entire $\Delta\phi$ range. If the like- and unlike-sign distributions

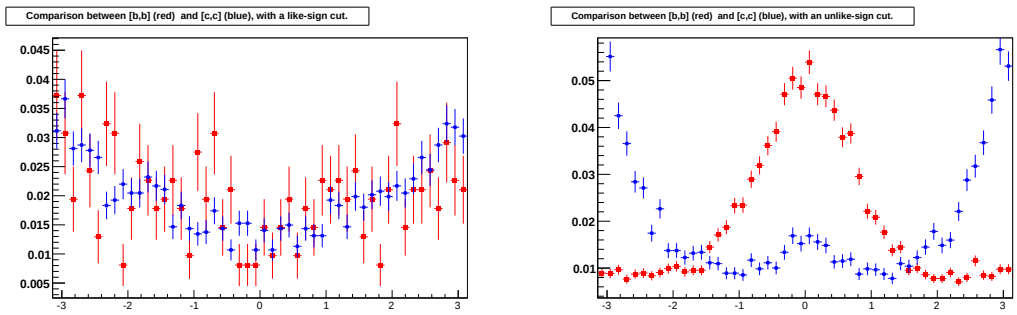

Figure 31: The left panel shows the $\Delta\phi$ distribution for $[b,b]$ (red) and $[c,c]$ (blue), with a like-sign cut. the $\Delta\phi$ distribution for $[b,b]$ (red) and $[c,c]$ (blue), with an unlike-sign cut. On the x-axis the $\Delta\phi$ in radians is depicted, while on the y-axis there is $\mathrm{d}N/\mathrm{d}\Delta\phi$ in rad^{-1}.

from this figure are added together for $[b,b]$ and $[c,c]$ respectively, the left plot from figure 30 would be found again. For the unlike-sign case for $[b,b]$, the small peak at the away-side has been successfully cut away. The small peak for $[c,c]$ at near-side is still visible. This is thus an improvement on the results when not using a sign cut. The conclusion from this is that with an unlike-sign cut $b\bar{b}$ can be enhanced on the near-side and $c\bar{c}$ on the away-side.
The next step is to look at where this small peak on the near-side in figure 31 in the right panel for $[c,c]$ comes from. For this reason the different process types and their respective shapes were studied, namely gluon splitting, pair creation and flavour excitation. From appendixes C.1- C.3 it can be clearly seen that all process types give similar $\Delta\phi$ distributions for the unlike-sign case. It is thus difficult to say which of the processes contributes to the small peak on the near-side for $[c,c]$ with unlike-sign cut and thus the separation of $b\bar{b}$ and $c\bar{c}$ is still difficult. It should also be noted that it is still unclear how one should distinguish between the different process types; as of yet no conclusive answer to this has been found. Each respective process types used in this

thesis is likely to contain other process types as well, although in a fairly limited amount.
The last step that will be taken is to study the $b\bar{b}$ purity on the near-side with an unlike-sign cut in place. This requires the study done on the minimum bias sample. The plots from appendix B.1 are used, although the scaling is done differently. A gross check is used, where we say that $N^{\text{trig}} = N_e^c + N_e^b$ is the factor we scale with. Here, N_e^c is the number of electrons coming from a c quark and N_e^b is the number of electrons coming from a b quark. The result is shown in figure 32. The number of electrons from b is a factor of four lower than the number of electrons from c.

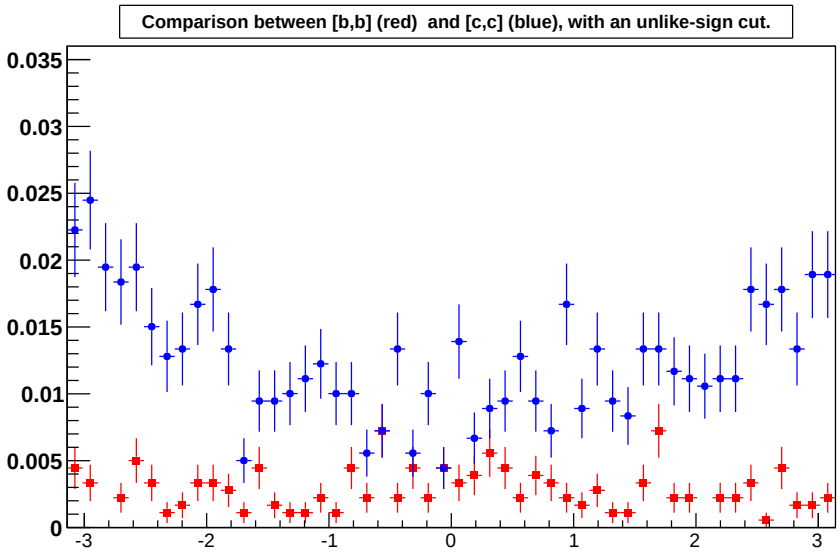

Figure 32: Plot of azimuthal correlation between electrons and charged D^* mesons, for the minimum bias sample with an unlike-sign cut in place and a scaling based on the total number of trigger electrons. [b,b] is marked in blue, [c,c] in red. On the x-axis the $\Delta\phi$ in radians is depicted, while on the y-axis there is $\mathrm{d}N/\mathrm{d}\Delta\phi$ in rad^{-1}.

The reason this distinction has not been seen yet in this analysis is because the previous results were only concerned with the shape of the distributions. On the near- and away side there is still a contribution from both sides (although in some cases relatively small) and the conclusion is therefore that with the current statistics, $b\bar{b}$ and $c\bar{c}$ cannot be separated fully, although it might be possible to enhance either one by looking at the near- or away-side with an unlike-sign cut in place. Furthermore, it was noted that the method used for determining process types are not yet fully developed and thus cannot be relied upon.

7 Conclusions

This thesis was concerned with charged D^* production in proton-proton and proton-lead collisions at $\sqrt{s} = 7$ and 5.02 TeV, respectively. In section 5 the yield extraction of the charged D^* meson was studied in proton-lead. First, an optimization of the topological cuts for the p_T range 1-2 GeV/c was done. After a method of iteration a set of cuts was found that looked optimal. Of course, because of the application of this method one cannot be sure whether the maximum found is a global maximum or in fact a local maximum of the significance in the multidimensional phase space of the topological cut parameters. After the determination of the sets of cuts per p_T bin, a study was done on the systematic error sources of the yield extraction. First, it was checked whether or not the Particle Identification cut worked as expected. Next, the background function and its parameters were changed in order to see whether or not the yield was stable under these modifications. Finally, the bin counting method was applied to the inverse mass spectra to determine how the yield changed when using this method. On the basis of the ratios of the yield for each method an estimate was done for the systematic error per p_T bin. Since a multidimensional optimization method might further improve the yield in the first bin, is this a step further research must take. An iterative method is handy in the beginning; because of the limited amount of computer memory it would cost a lot of processing power to vary all topological cut parameters at the same time.
In section 6 an azimuthal correlation method between electrons and charged D^* mesons was studied, in particular the feasibility to apply this method in the seperation of $b\bar{b}$ and $c\bar{c}$ contributions. An enhanced- and a minimum bias data sample was used for this analysis. From the enhanced data sample it was concluded that an unlike-sign cut can enhance $b\bar{b}$ on the near-side and $c\bar{c}$ on the away side. Next, it was determined that one cannot know the origin of the small peak at near-side for the case that the electrons comes from a c quark and the D^* meson comes from a c quark as well. This because the process types gluon splitting, pair creation and flavour excitation have the same $\Delta\phi(e-D^*)$ distributions. Also, with current methods these process types cannot be separated well enough. Finally, a minimum bias study was done in order to determine the $b\bar{b}$ purity on the near-side with an unlike-sign cut in place. The result from this study showed more statistics are needed in order to say if this correlation method can be used for the separation of $b\bar{b}$ and $c\bar{c}$ contributions.

A Enhanced Sample

A.1 Heavy Flavour with detector effects

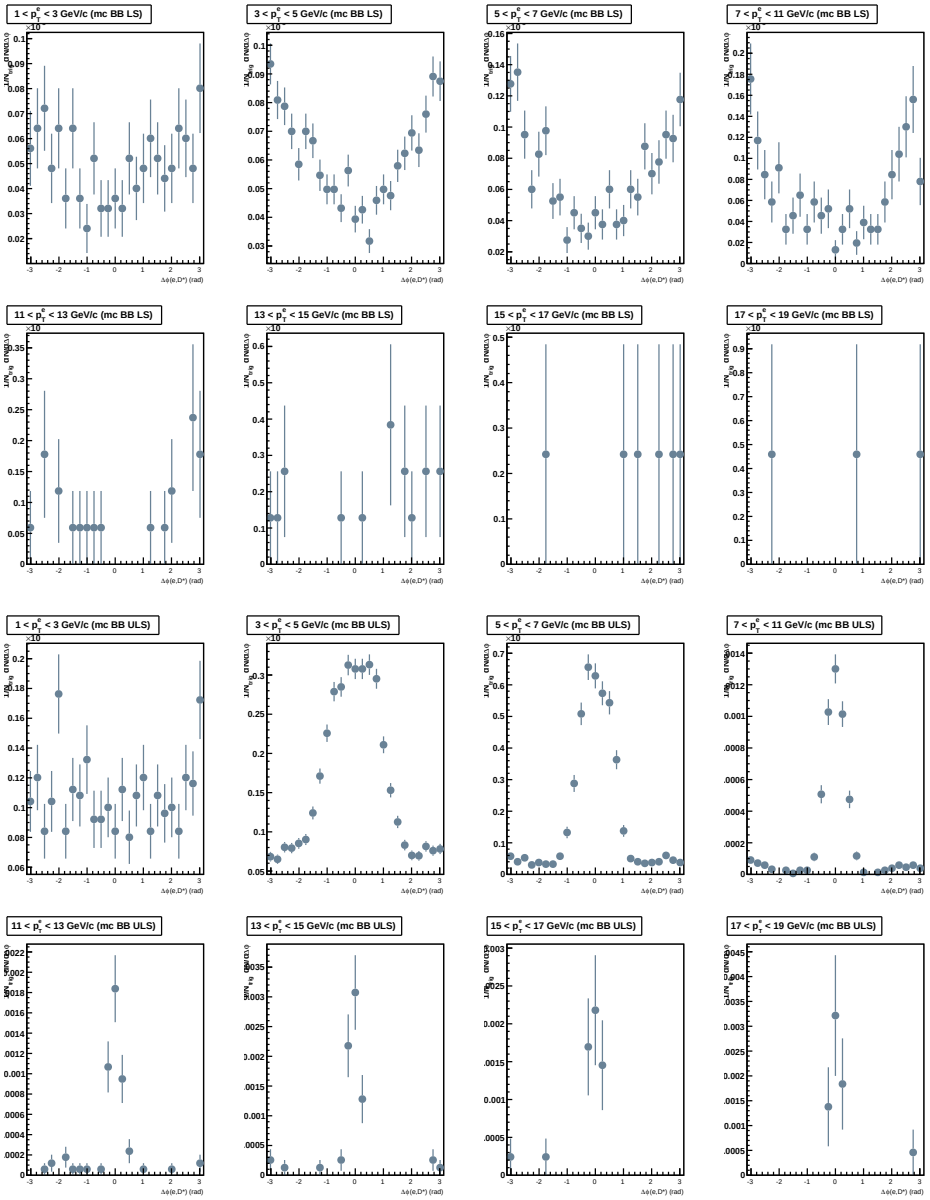

Figure 33: The upper eight panels show the $[b, b]$ like-sign correlation, the lower eight depict the $[b, b]$ unlike-sign correlation. On the x-axis the $\Delta\phi$ in radians is depicted, while on the y-axis there is $\mathrm{d}N/\mathrm{d}\Delta\phi$ in rad^{-1}.

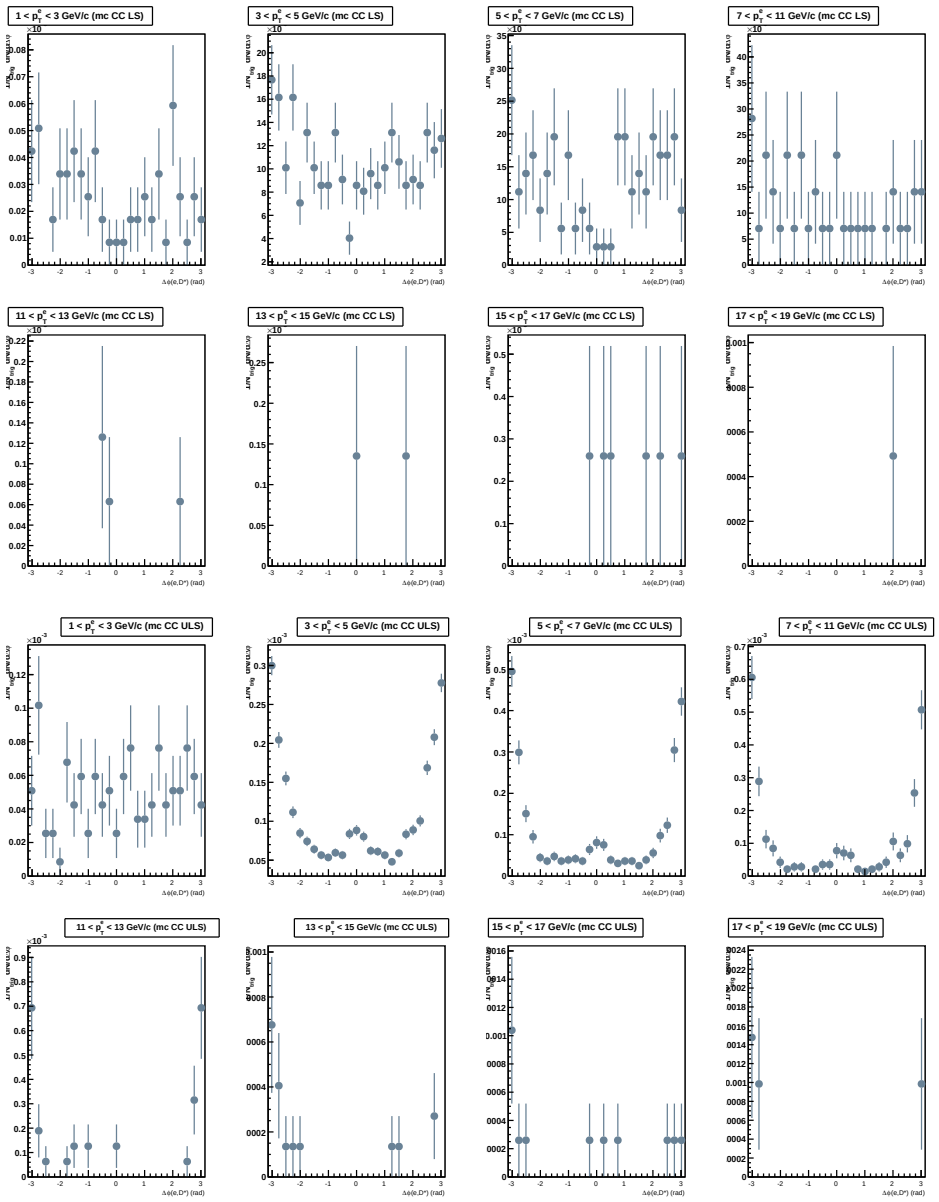

Figure 34: The upper eight panels are $[c, c]$ like-sign, the lower eight panels show $[c, c]$ unlike-sign. On the x-axis the $\Delta\phi$ in radians is depicted, while on the y-axis there is $\mathrm{d}N/\mathrm{d}\Delta\phi$ in rad^{-1}.

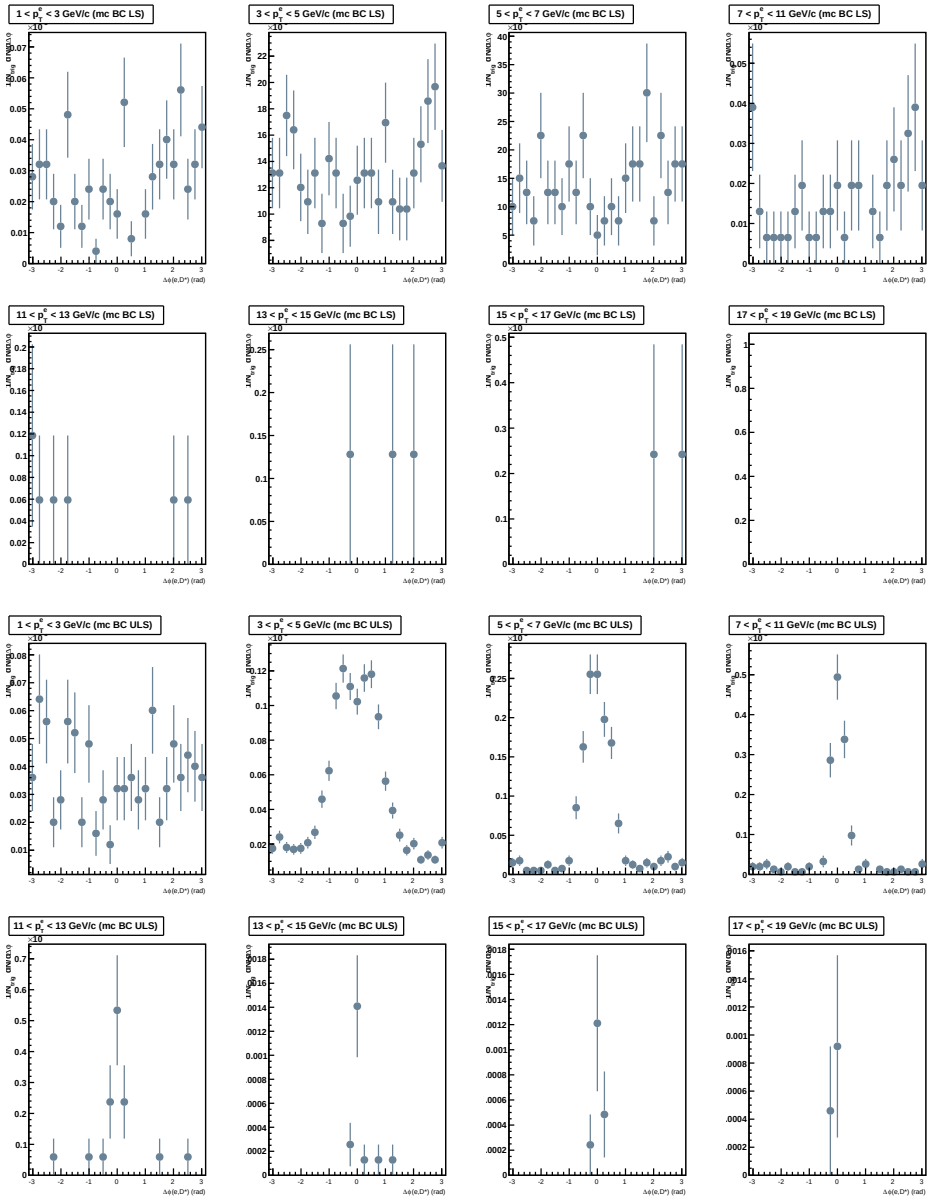

Figure 35: The upper eight panels are $[b, c]$ like-sign, the lower eight panels are $[b, c]$ unlike-sign correlations. On the x-axis the $\Delta\phi$ in radians is depicted, while on the y-axis there is $\mathrm{d}N/\mathrm{d}\Delta\phi$ in rad^{-1}.

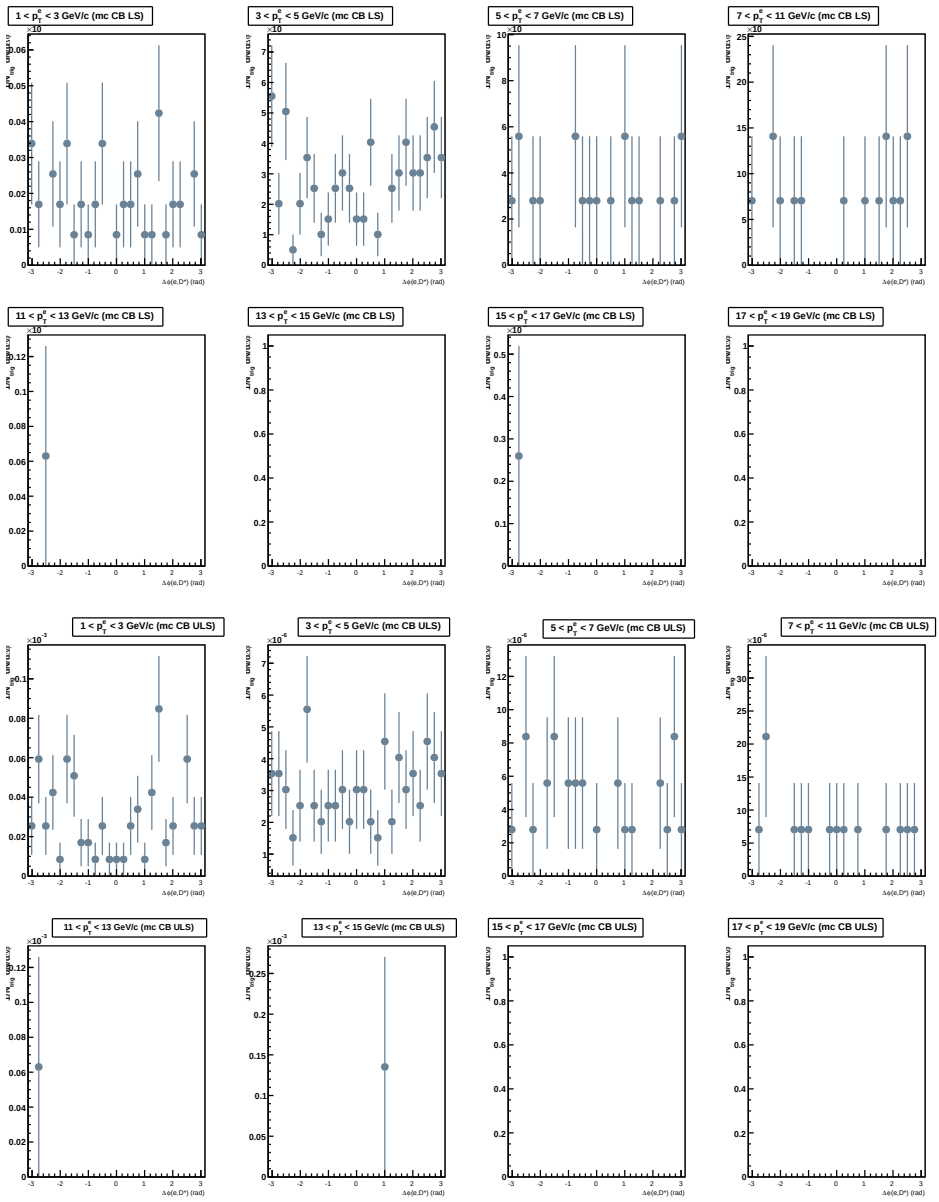

Figure 36: The upper eight panels are $[c, b]$ like-sign, the lower eight panels are $[c, b]$ unlike-sign. On the x-axis the $\Delta\phi$ in radians is depicted, while on the y-axis there is $\mathrm{d}N/\mathrm{d}\Delta\phi$ in rad^{-1}.

A.2 Heavy Flavour without detector effects

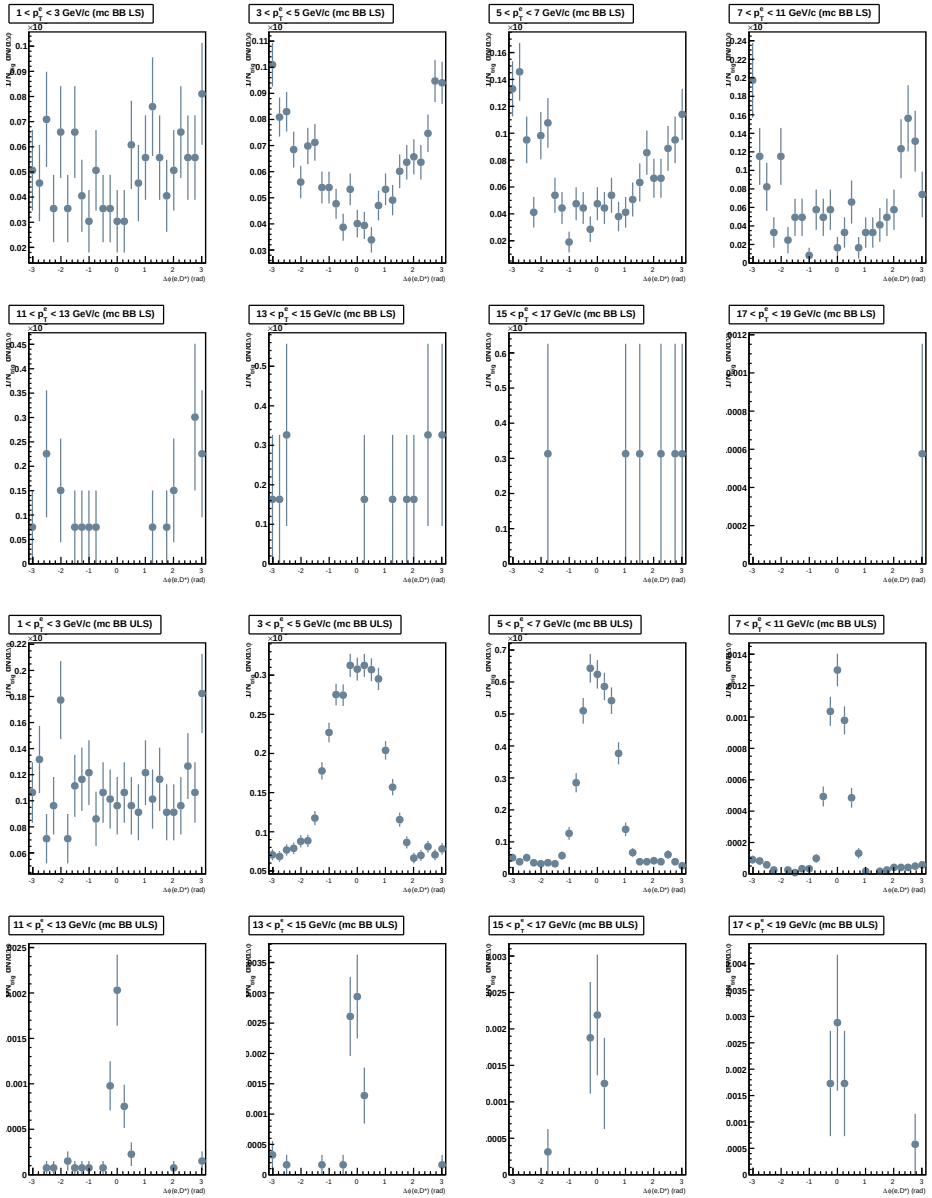

Figure 37: The upper eight panels show the $[b, b]$ like-sign correlation, the lower eight panels are $[b, b]$ unlike-sign correlations. On the x-axis the $\Delta\phi$ in radians is depicted, while on the y-axis there is $\mathrm{d}N/\mathrm{d}\Delta\phi$ in rad^{-1}.

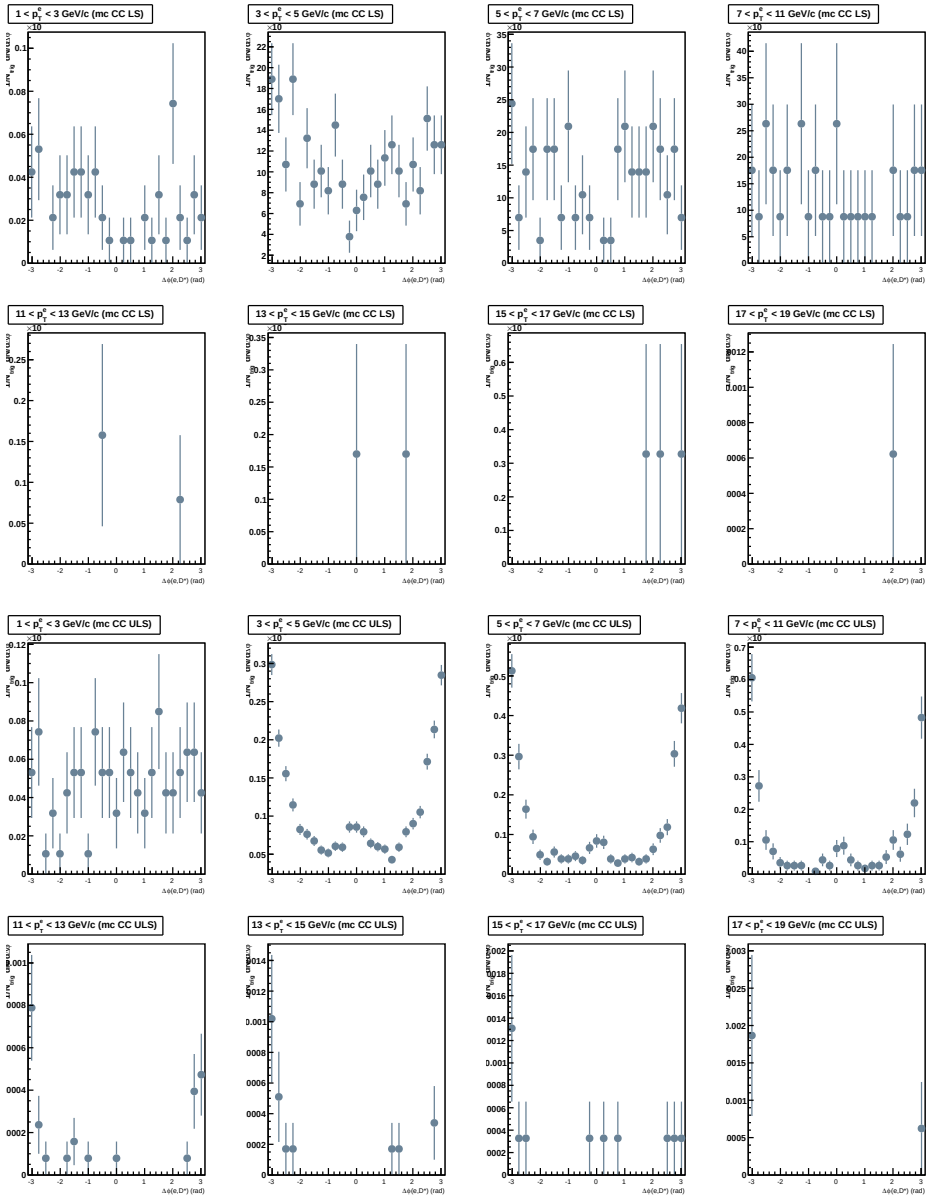

Figure 38: The upper eight panels are $[c, c]$ like-sign correlations, the lower eight panels depict the $[c, c]$ unlike-sign correlations. On the x-axis the $\Delta\phi$ in radians is depicted, while on the y-axis there is $\mathrm{d}N/\mathrm{d}\Delta\phi$ in rad^{-1}.

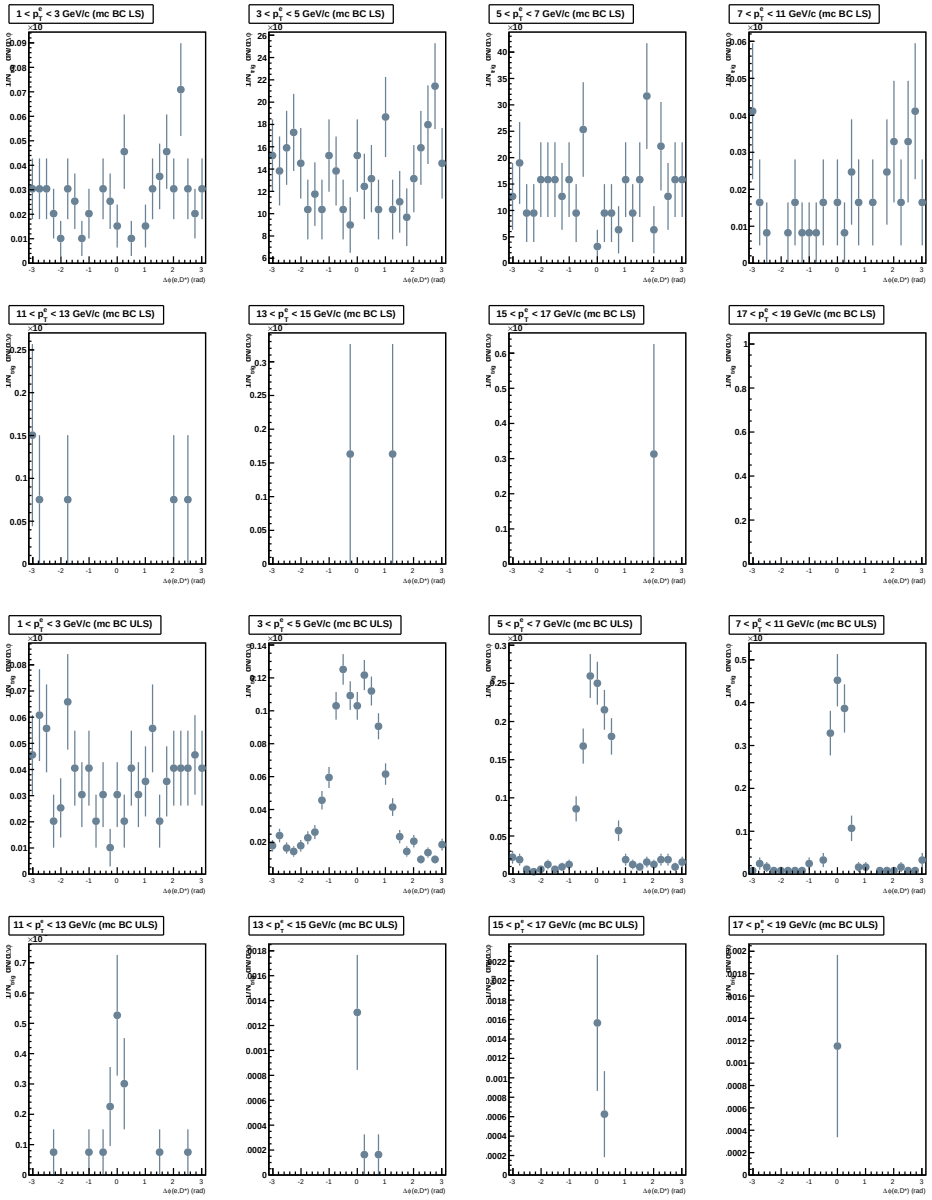

Figure 39: The upper eight panels are $[b, c]$ like-sign correlations, the lower eight panels are $[b, c]$ unlike-sign correlations. On the x-axis the $\Delta\phi$ in radians is depicted, while on the y-axis there is $\mathrm{d}N/\mathrm{d}\Delta\phi$ in rad^{-1}.

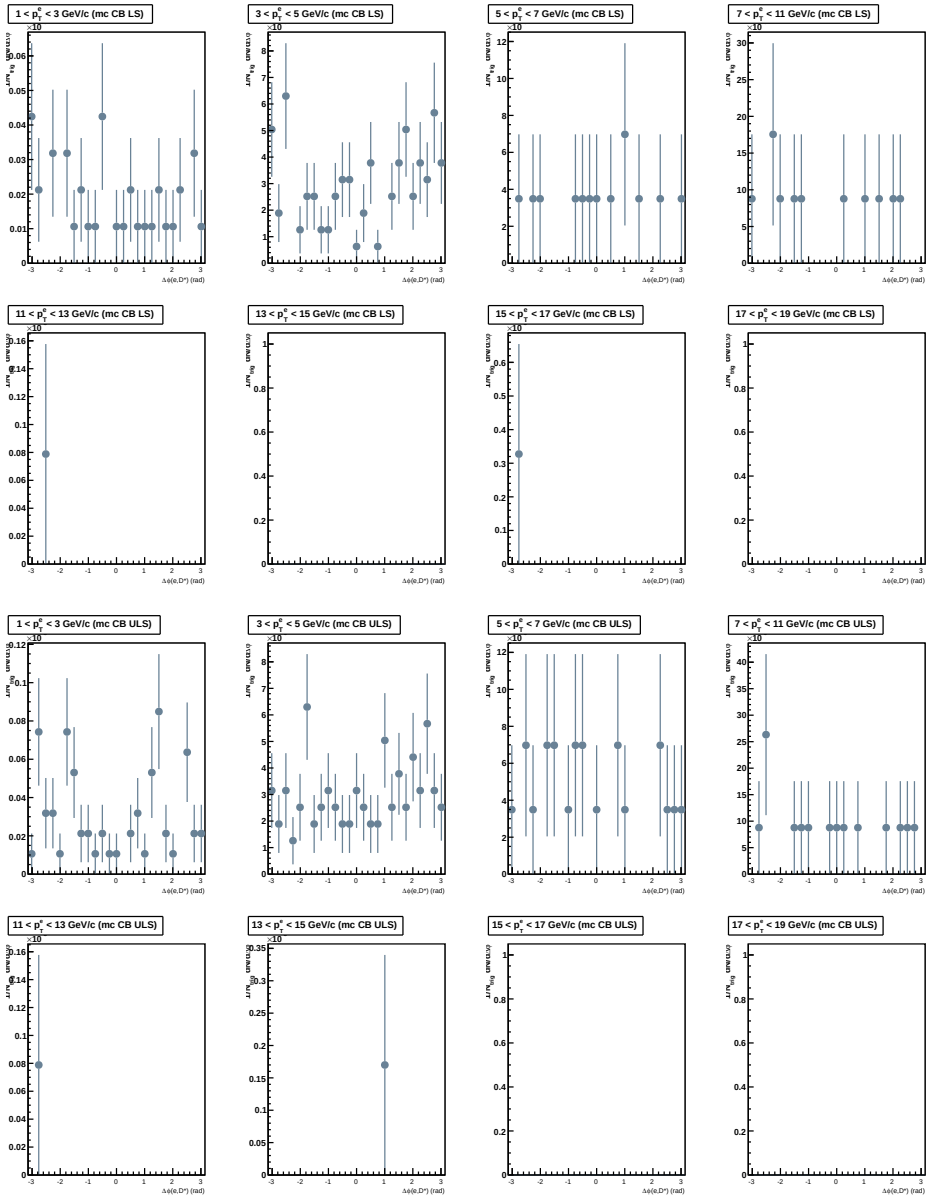

Figure 40: The upper eight panels are $[c, b]$ like-sign correlations, the lower eight panels show the $[c, b]$ unlike-sign correlations. On the x-axis the $\Delta\phi$ in radians is depicted, while on the y-axis there is $\mathrm{d}N/\mathrm{d}\Delta\phi$ in rad^{-1}.

A.3 Non-Heavy Flavour with detector effects

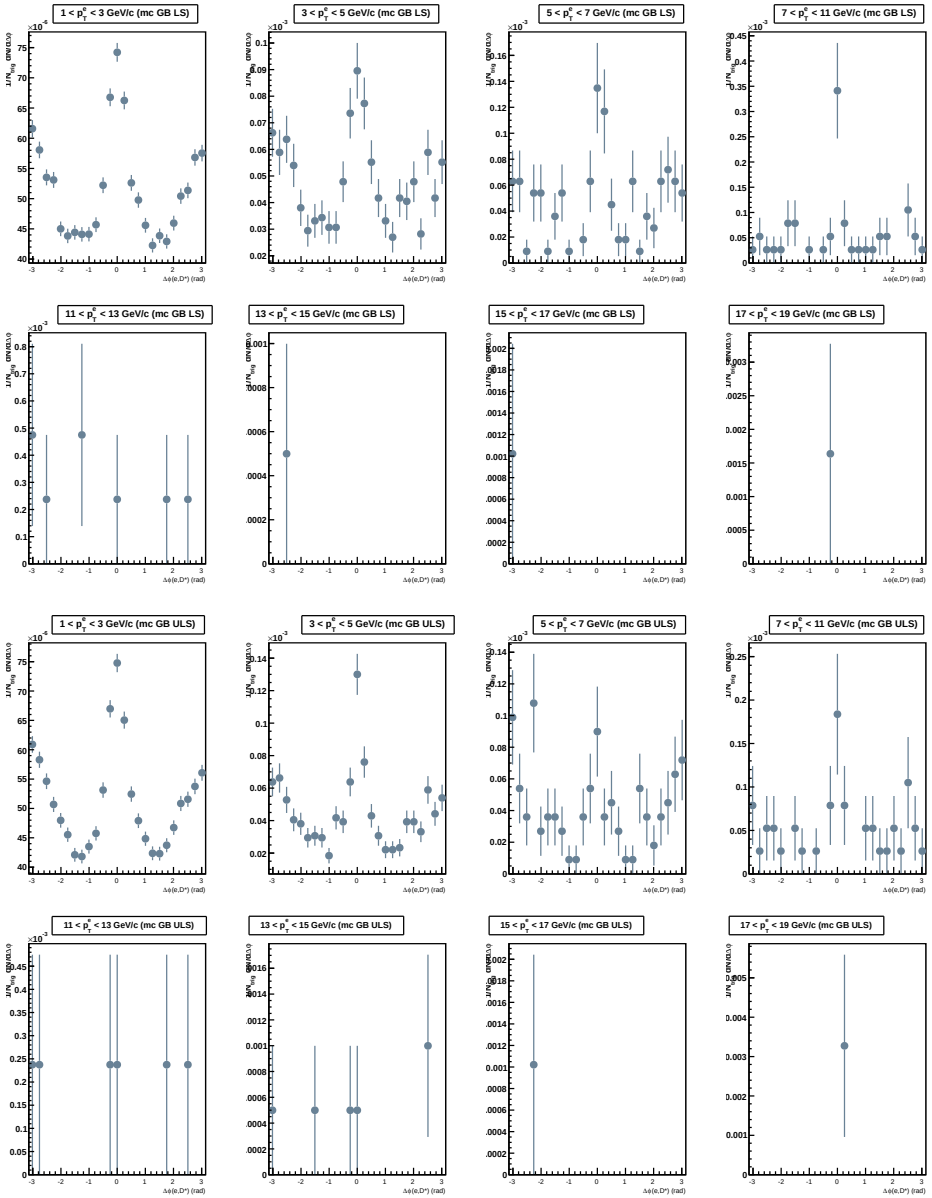

Figure 41: The upper eight panels show the $[\gamma, b]$ like-sign correlations, the lower eight are $[\gamma, b]$ unlike-sign correlations. On the x-axis the $\Delta\phi$ in radians is depicted, while on the y-axis there is $\mathrm{d}N/\mathrm{d}\Delta\phi$ in rad^{-1}.

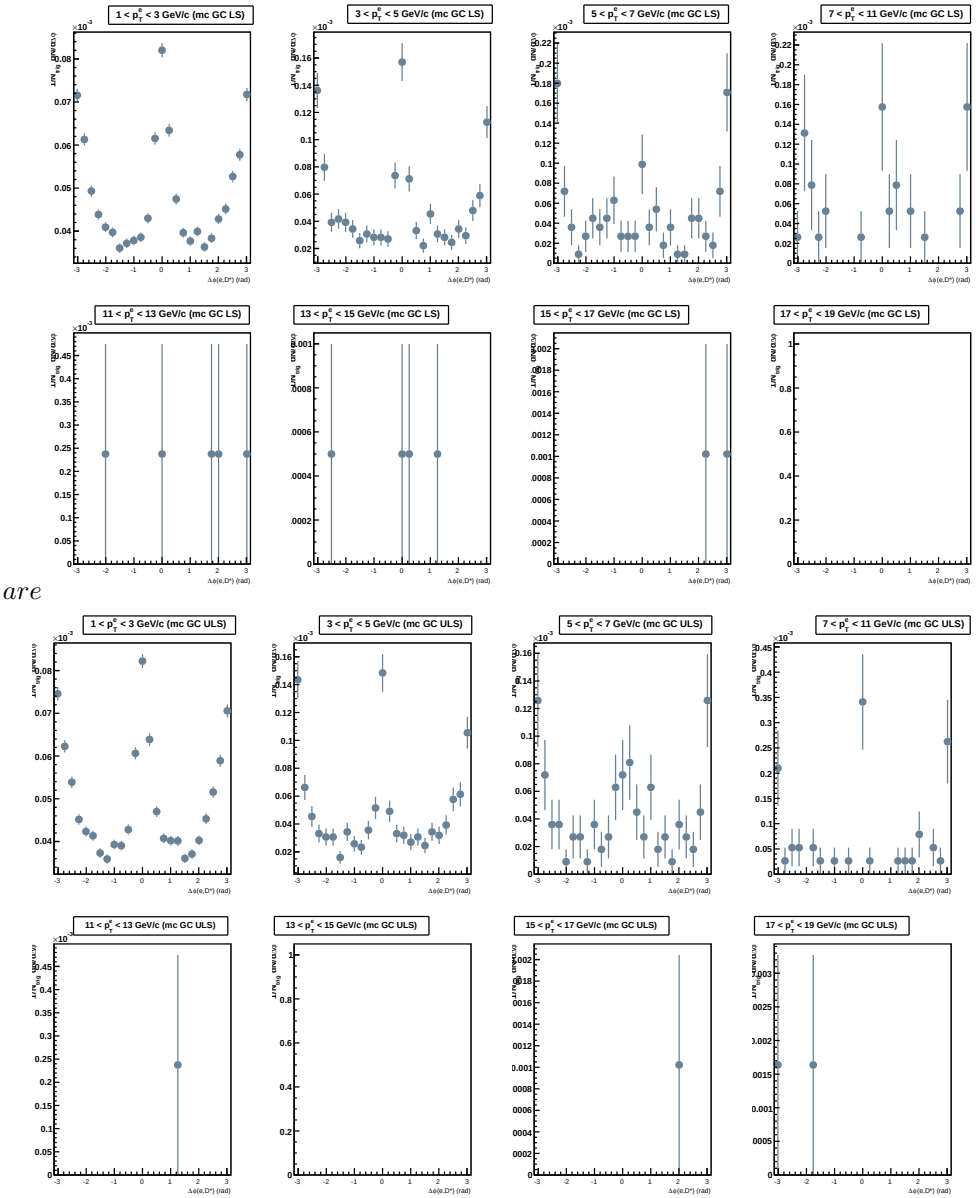

are

Figure 42: The upper eight panels are $[\gamma, c]$ like-sign correlations, the lower eight are $[\gamma, c]$ unlike-sign correlations. On the x-axis the $\Delta\phi$ in radians is depicted, while on the y-axis there is $\mathrm{d}N/\mathrm{d}\Delta\phi$ in rad^{-1}.

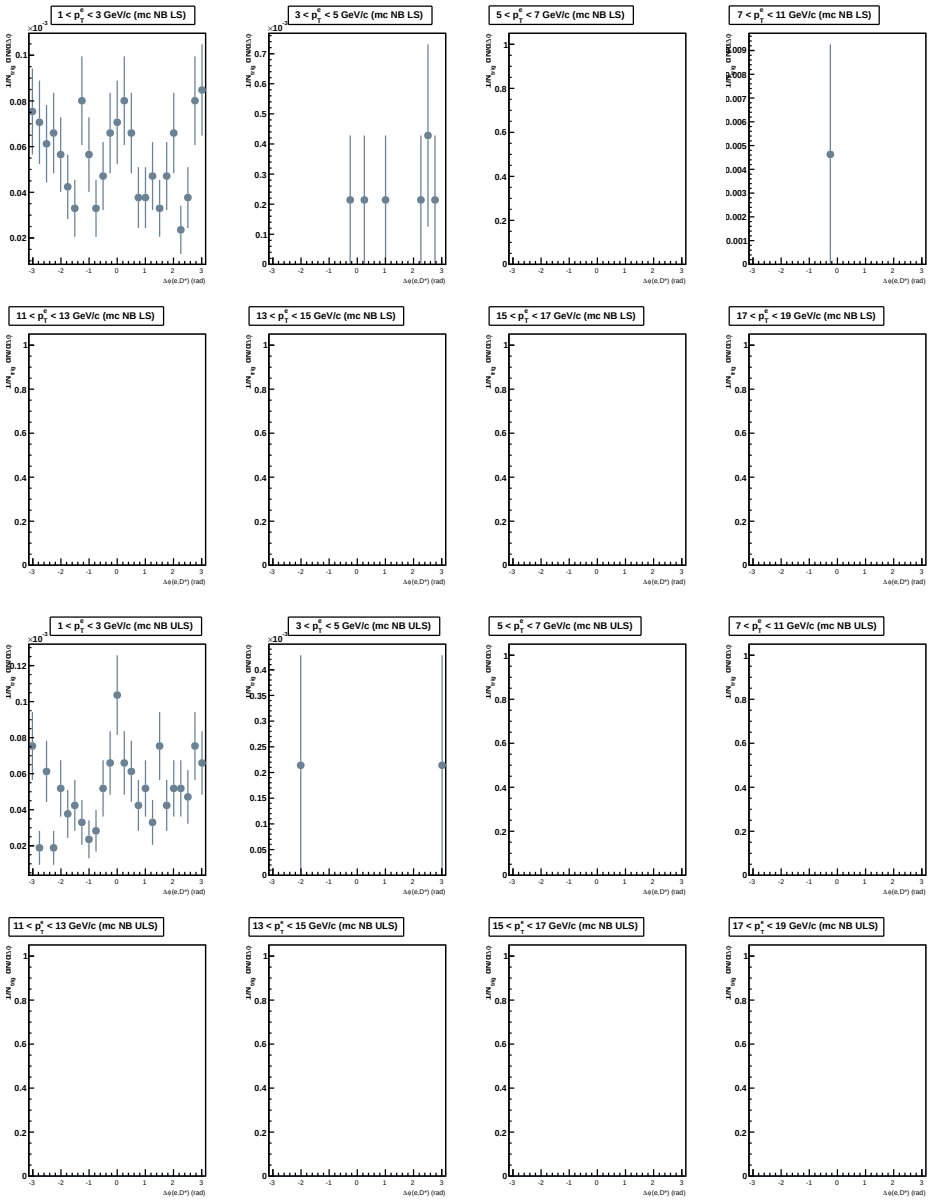

Figure 43: Take X to be π^0 or η. Then the upper eight panels are $[X, b]$ like-sign correlations, the lower eight are $[X, b]$ unlike-sign correlations. On the x-axis the $\Delta\phi$ in radians is depicted, while on the y-axis there is $\mathrm{d}N/\mathrm{d}\Delta\phi$ in rad^{-1}.

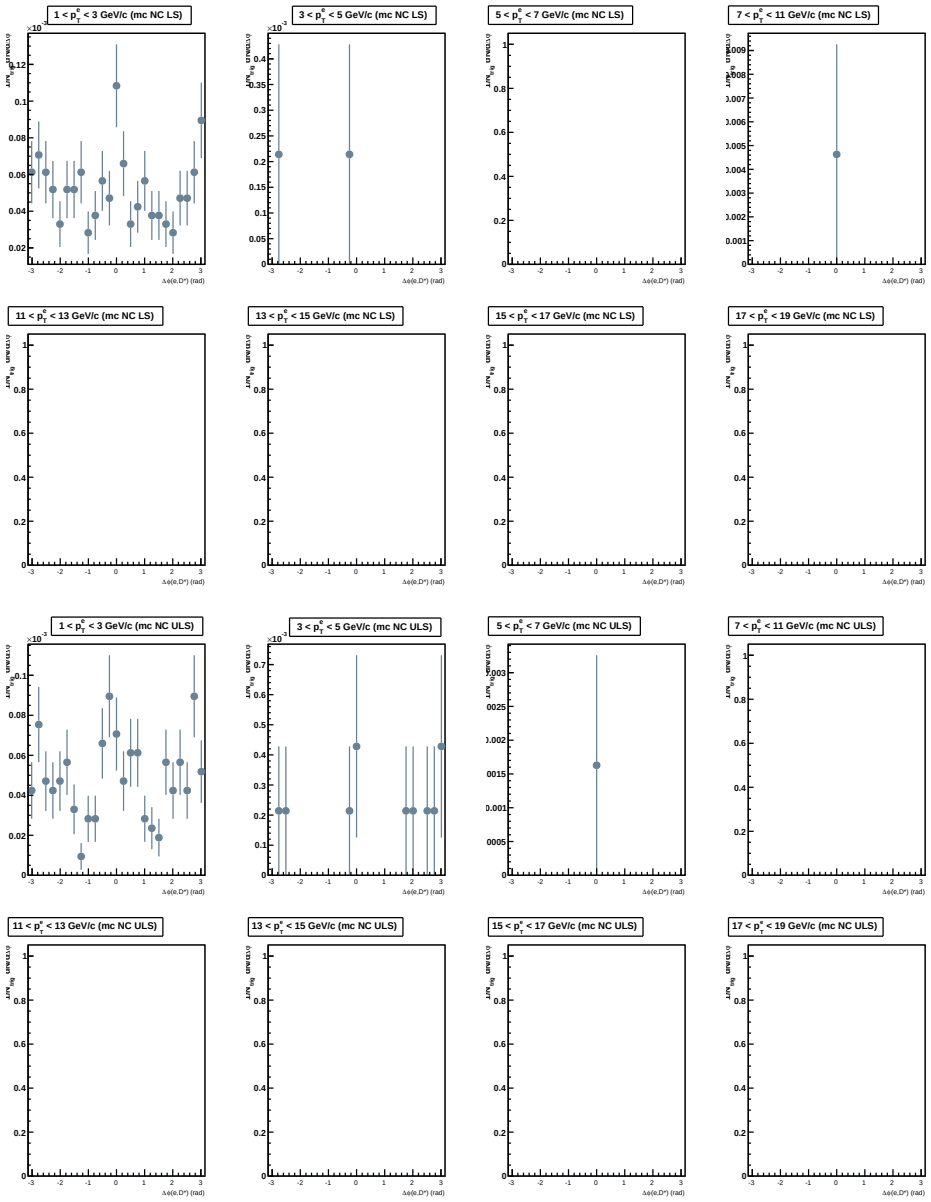

Figure 44: Take X to be π^0 or η. Then the upper eight panels are $[X, c]$ like-sign, the lower eight are $[X, c]$ unlike-sign. On the x-axis the $\Delta\phi$ in radians is depicted, while on the y-axis there is $\mathrm{d}N/\mathrm{d}\Delta\phi$ in rad^{-1}.

A.4 Non-Heavy Flavour without detector effects

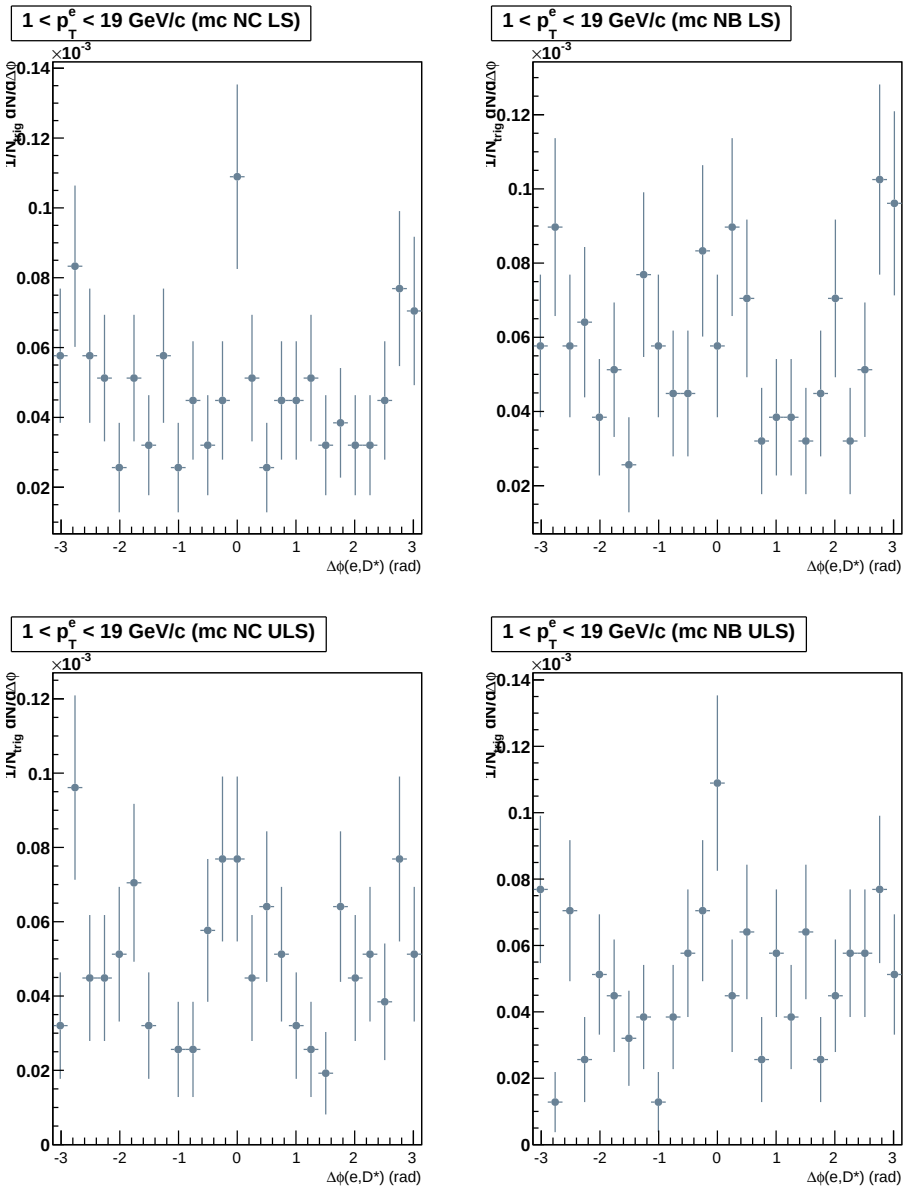

Figure 45: Take X to be π^0 or η. Then the upper two panels are $[X, c]$ and $[X, b]$ like-sign correlations respectively, the lower eight panels are $[X, c]$ and $[X, b]$ unlike-sign correlations respectively. On the x-axis the $\Delta\phi$ in radians is depicted, while on the y-axis there is $\mathrm{d}N/\mathrm{d}\Delta\phi$ in rad^{-1}.

B Minimum Bias Sample

B.1 Heavy Flavour correlation with η_e cut

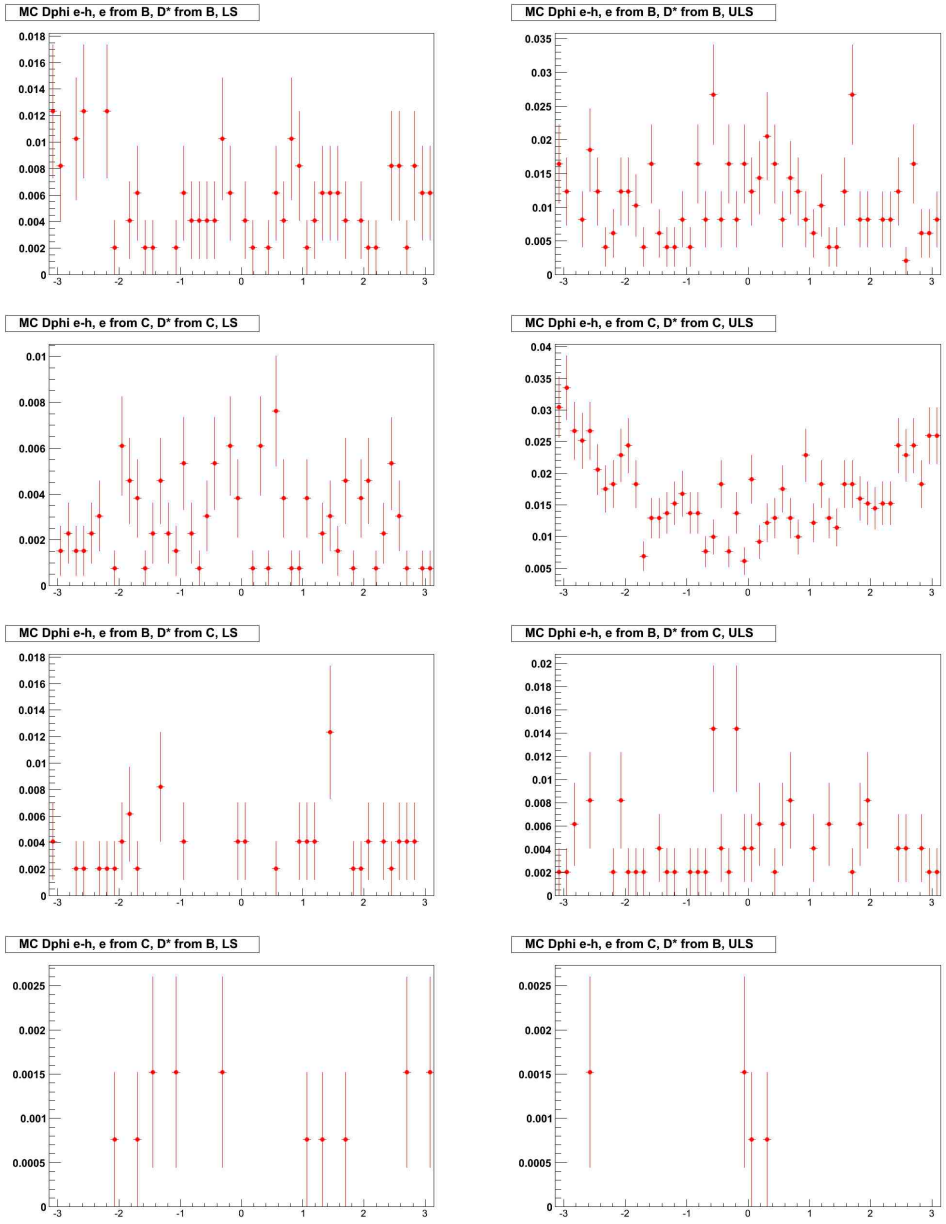

Figure 46: Results for the azimutal correlation between electrons and charged D^* mesons for the minimum bias sample, p_T integrated and with $|\eta_e| < 1$. Electrons do not originate from reactions with the detector. On the x-axis the $\Delta\phi$ in radians is depicted, while on the y-axis there is $dN/d\Delta\phi$ in rad^{-1}.

C Process Types

C.1 Gluon Splitting

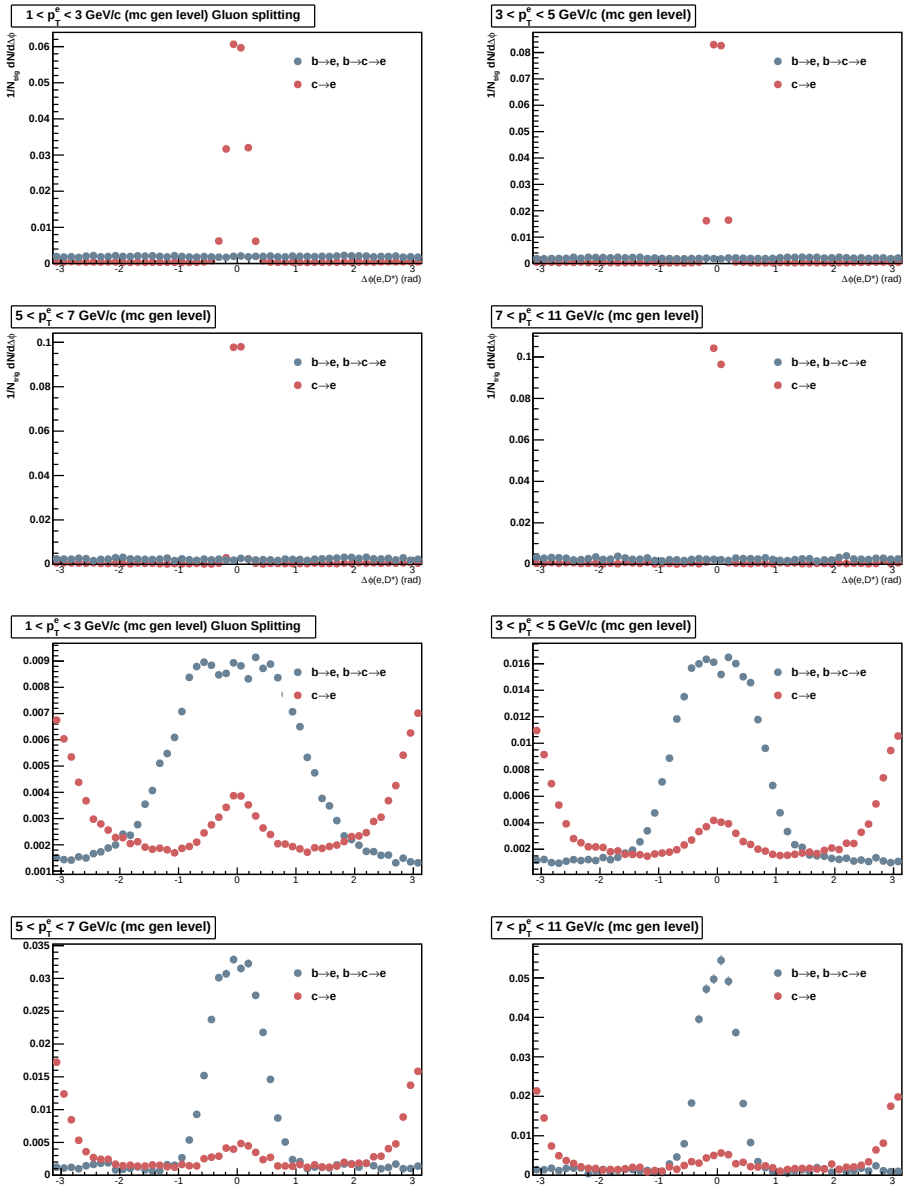

Figure 47: The upper four panels show the like-sign $e-\mathrm{D}^*$ correlation for gluon splitting. The lower four show the unlike-sign $e-\mathrm{D}^*$ correlation for gluon splitting. On the x-axis the $\Delta\phi$ in radians is depicted, while on the y-axis there is $\mathrm{d}N/\mathrm{d}\Delta\phi$ in rad^{-1}.

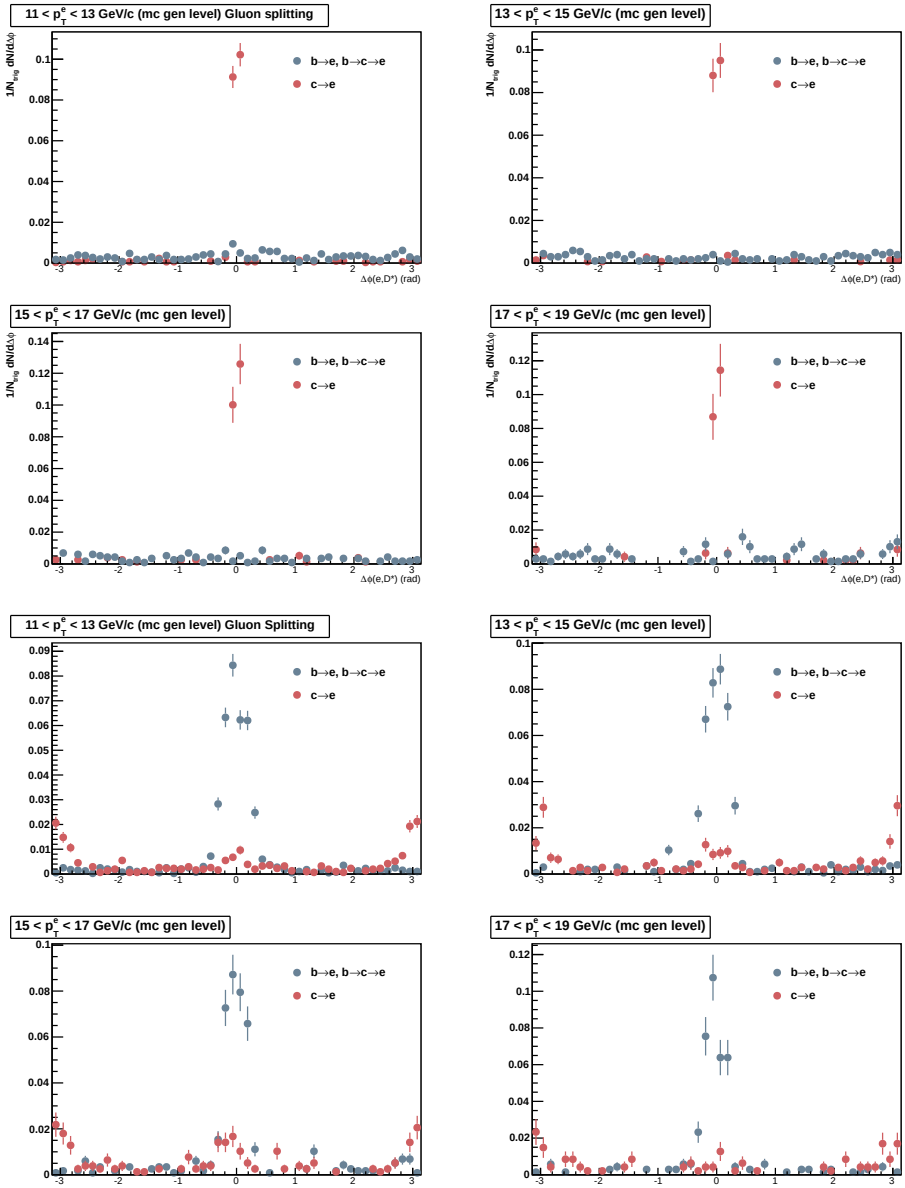

Figure 48: The upper four show the like-sign $e-\mathrm{D}^*$ correlation for gluon splitting. The lower four depict the unlike-sign $e-\mathrm{D}^*$ correlation for gluon splitting. On the x-axis the $\Delta\phi$ in radians is depicted, while on the y-axis there is $\mathrm{d}N/\mathrm{d}\Delta\phi$ in rad^{-1}.

C.2 Flavour Excitation

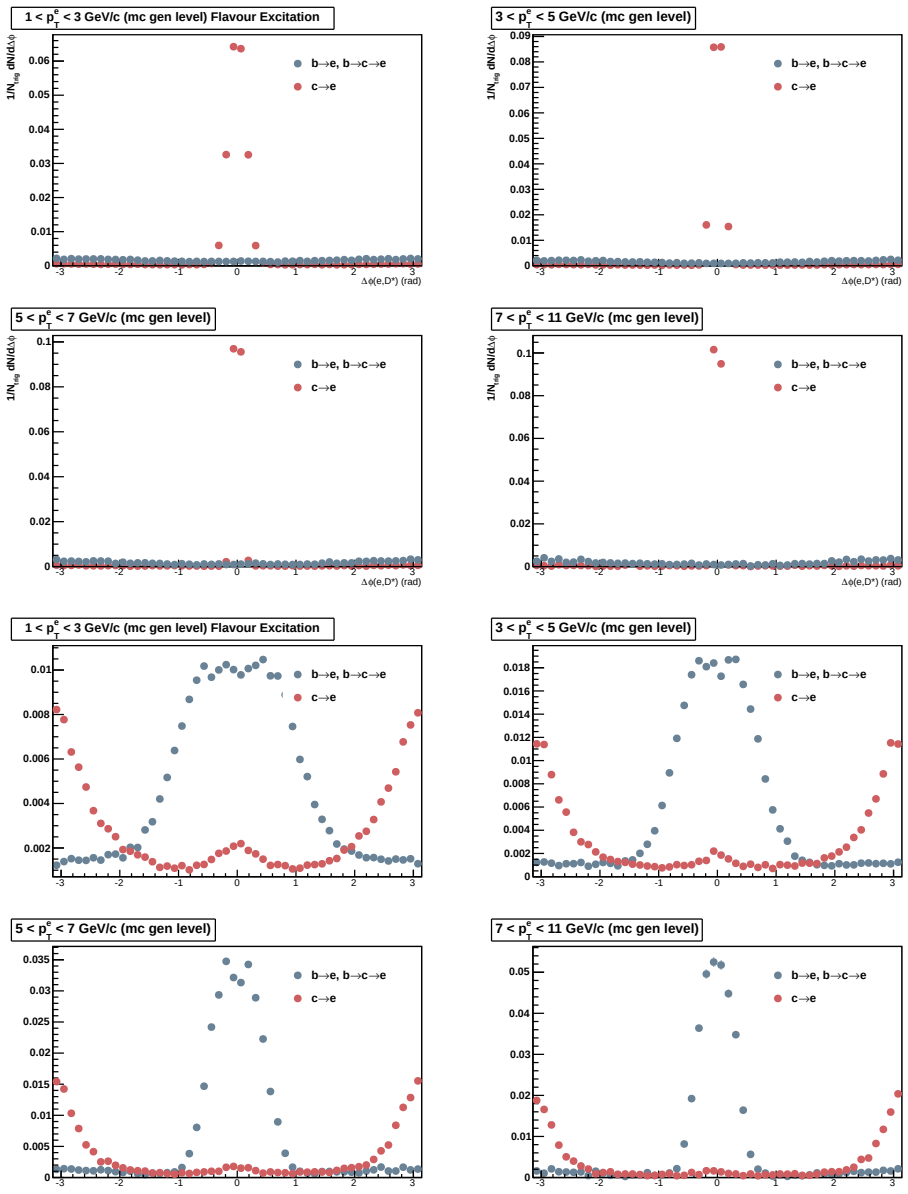

Figure 49: The upper four panels show the like-sign $e-\mathrm{D}^*$ correlation for flavour excitation. The lower four panels show the unlike-sign $e-\mathrm{D}^*$ correlation for flavour excitation. On the x-axis the $\Delta\phi$ in radians is depicted, while on the y-axis there is $\mathrm{d}N/\mathrm{d}\Delta\phi$ in rad^{-1}.

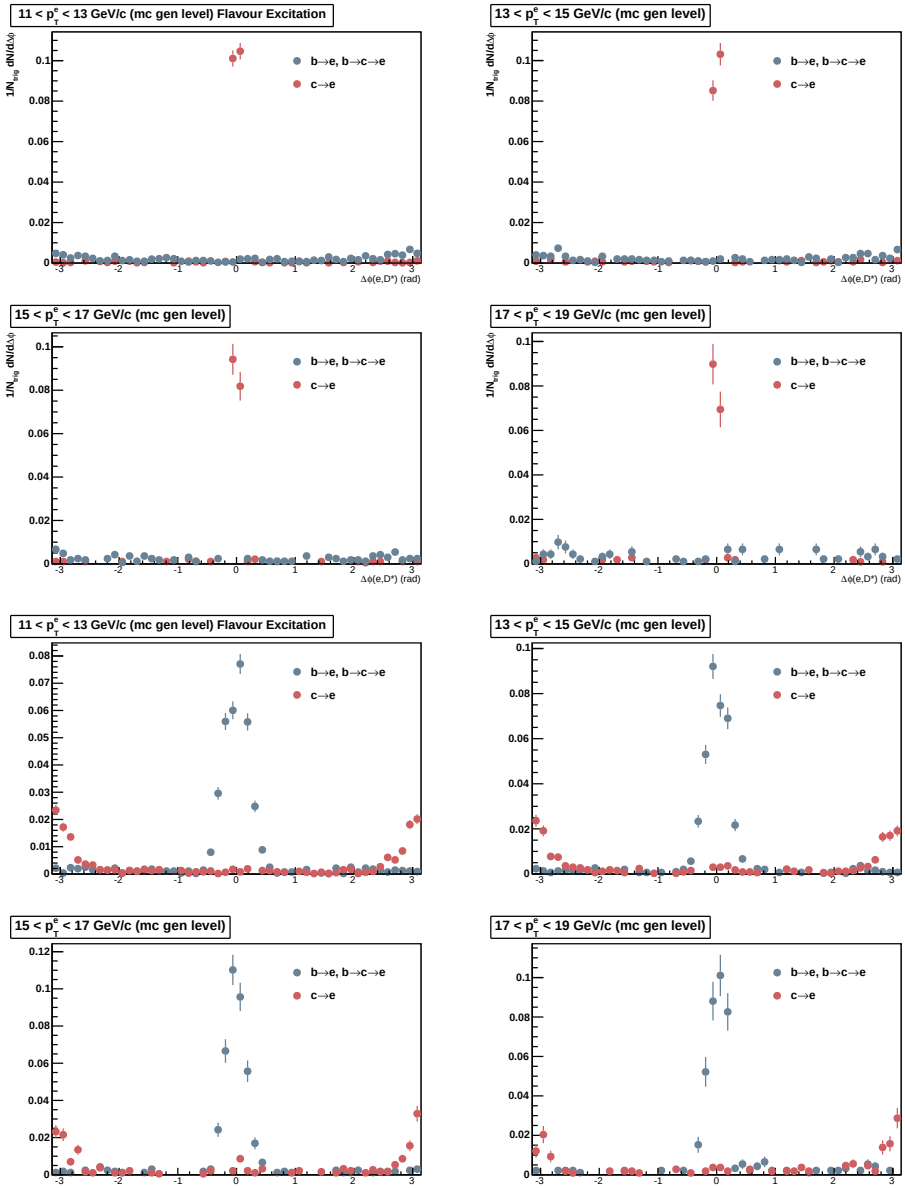

Figure 50: The upper four panels show the like-sign $e-\mathrm{D}^*$ correlation for flavour excitation. The lower four panels show the unlike-sign $e-\mathrm{D}^*$ correlation for flavour excitation. On the x-axis the $\Delta\phi$ in radians is depicted, while on the y-axis there is $\mathrm{d}N/\mathrm{d}\Delta\phi$ in rad^{-1}.

C.3 Pair Creation

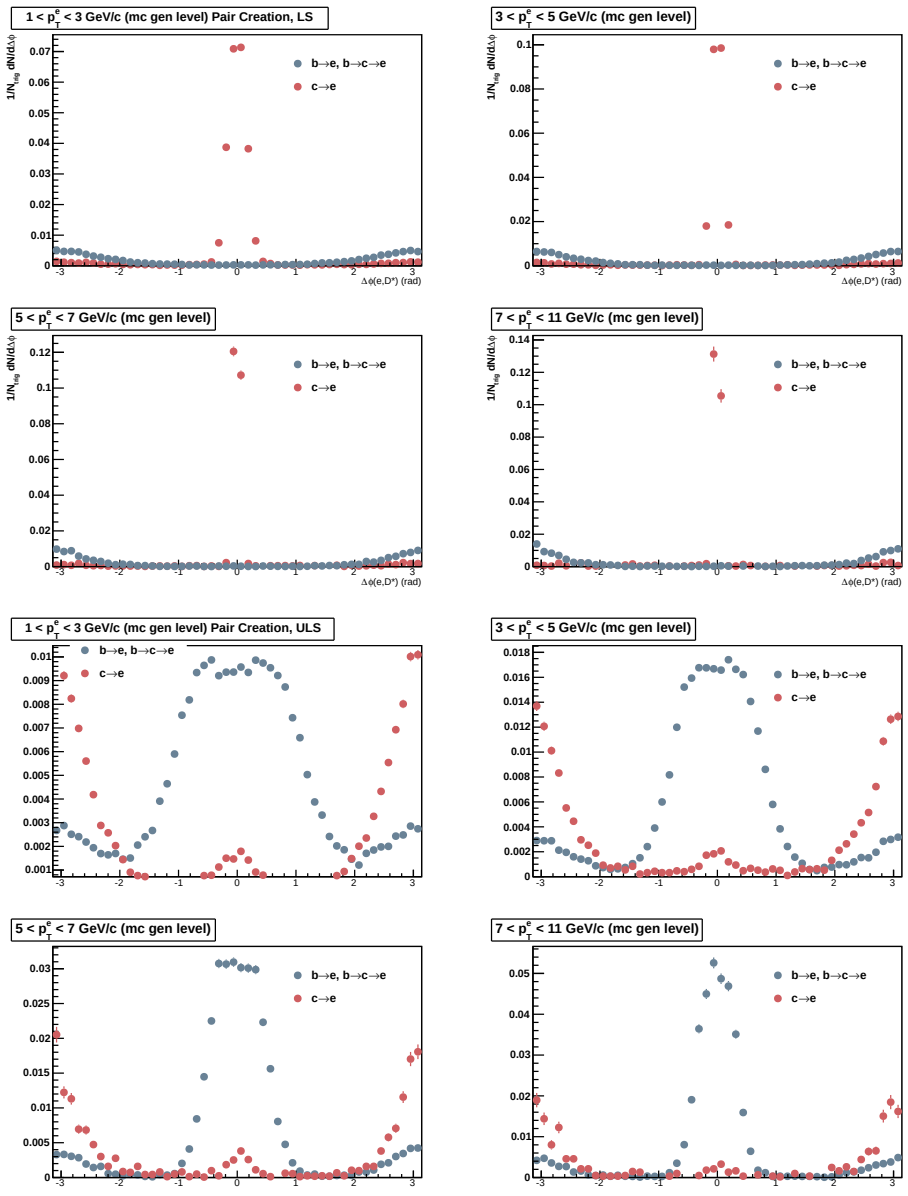

Figure 51: The upper four panels show the like-sign $e-\mathrm{D}^*$ correlation for pair creation. The lower four panels show the unlike-sign $e-\mathrm{D}^*$ correlation for pair creation. On the x-axis the $\Delta\phi$ in radians is depicted, while on the y-axis there is $\mathrm{d}N/\mathrm{d}\Delta\phi$ in rad^{-1}.

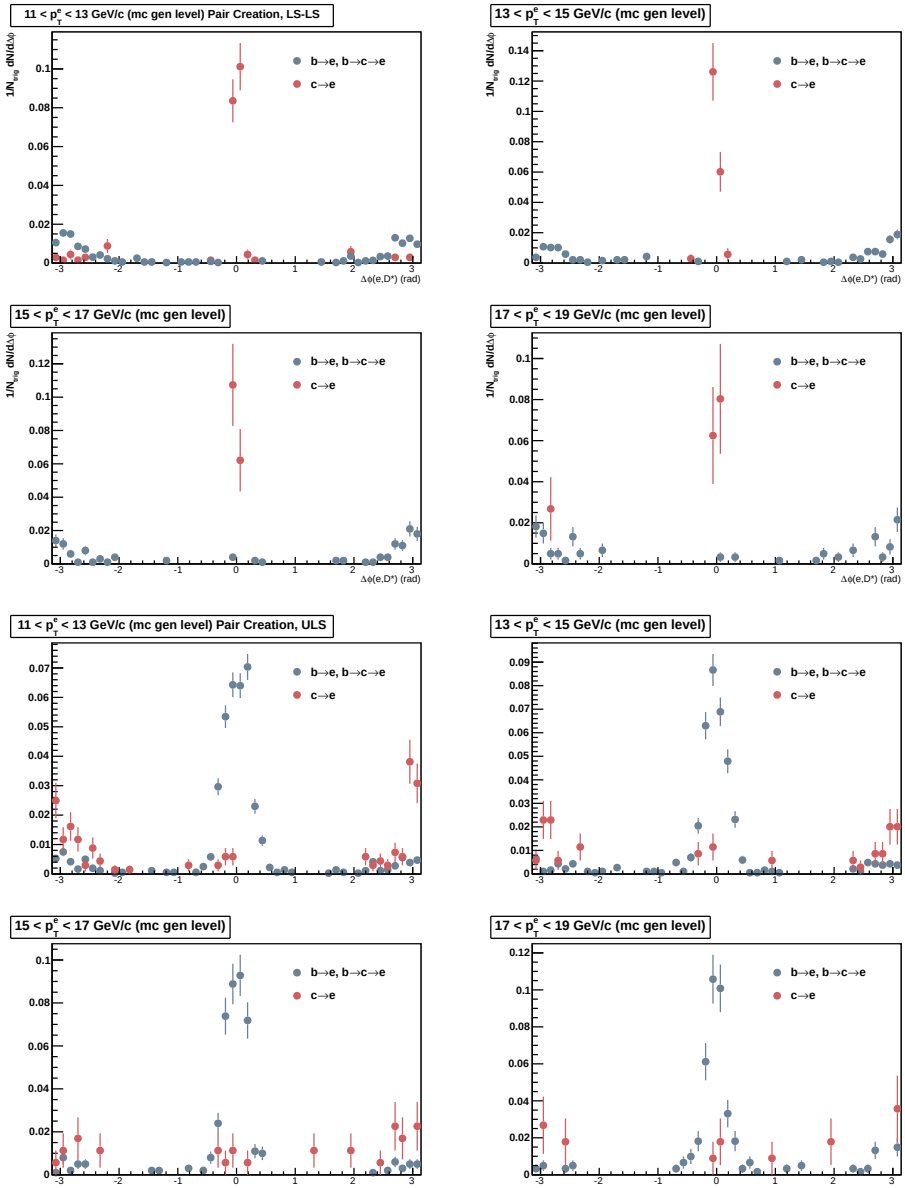

Figure 52: The upper four panels show the like-sign $e-\mathrm{D}^*$ correlation for pair creation. The lower four show the unlike-sign $e-\mathrm{D}^*$ correlation for pair creation. On the x-axis the $\Delta\phi$ in radians is depicted, while on the y-axis there is $\mathrm{d}N/\mathrm{d}\Delta\phi$ in rad^{-1}.

A References

[1] D. Griffiths, *Introduction to Elementary Particles*. Wiley-VCH, 2nd Edition, 2008.

[2] T. Frängsmyr, *Les Prix Nobel*. The Nobel Prices 1999, Stockholm, Sweden, 2000.

[3] R.S. de Rooij, *Prompt D^{*+} production in proton-proton and lead-lead collisions, measured with the ALICE experiment at the CERN Large Hadron Collider*. University of Utrecht, Utrecht, The Netherlands, 2013.

[4] J. Beringer et al. (Particle Data Group), PR D86 010001 (2012). `http://pdg.lbl.gov`

[5] A. Grelli for the ALICE collaboration, proceedings for the Quark Matter conference, submitted to Nucl. Phys. A, October 2012.

[6] B.I. Abelev et al., Journal of High Energy Physics 9, 112 (2012).

[7] B.I. Abelev et al., Journal of High Energy Physics 01, 128 (2012).

[8] B.I. Abelev et al., Journal of High Energy Physics 07, 191 (2012).

[9] W.M. Alberico et al., Eur. Phyis J. C 71, 1666 (2011).

[10] N. Armesto, A. Dainese, C.A. Salgado and U.A. Wiedermann, Phys. Rev. D 71, 054027 (2005).

[11] O. Fochler, J. Uphoff, Z. Xu and C. Greiner, J. Phys. G: Nucl. Part. Phys. 38, 124152 (2011).

[12] P.B. Gossiaux, R. Bierkandt and J. Aichelin, Phys. Rev. C 79, 044906 (2009).

[13] M. He, R.J. Fries and R. Rapp, arXiv: 1204.4442.

[14] W.A. Horowitz and M. Gyulassy, J. Phys. G: Nucl. Part. Phys. 38, 124114 (2011).

[15] R. Sharma, I. Vitev and B.W. Zhang, Phys. Rev. C 80, 054902 (2009); Y. He, I. Vitev and B.W. Zhang, arXiv: 1105.2566 (2011).

[16] B. Abelev et al., *Pseudorapidity distribution of charged particles in p-Pb collisions at $\sqrt{s_{NN}} = 5.02$ TeV*, Phys. Rev. Lett. 110, 082302 (2013).

[17] D. Thomas, S. Lapointe, A. Mischke, E. Pereira de Oliveira Filho, A.A.P. Suaide, *Azimuthal angular correlations of heavy flavour decay electrons and charged hadrons in proton-proton collisions at $\sqrt{s} = 2.76$ TeV using the ALICE detector*, 2012.

[18] A. Mischke, *A new correlation method to identify and separate charm and bottom production processes at RHIC*, arXiv: 0807.1309v4 (2009).